PEDRO DAVID ARSÉNIO COPETO

BSc in Physics Engineering

LIGHT FRAGMENT DETECTION USING RESISTIVE PLATE CHAMBERS

CONTRIBUTION TO GSI EXPERIMENT G249

DEPARTMENT OF
PHYSICS

LIGHT FRAGMENT DETECTION USING RESISTIVE PLATE CHAMBERS

CONTRIBUTION TO GSI EXPERIMENT G249

PEDRO DAVID ARSÉNIO COPETO

BSc in Physics Engineering

Adviser: Daniel Galaviz Redondo
Assistant Professor, University of Lisbon

Co-adviser: João Duarte Neves Cruz
Associate Professor, NOVA University Lisbon

Light fragment detection using Resistive Plate Chambers
Contribution to GSI experiment G249

ACKNOWLEDGEMENTS

First and foremost, I would like to express my sincere gratitude to my advisor, Professor Daniel Galaviz, not only for his guidance and support throughout this thesis, but also for being my first entry point into the research world of nuclear physics. From the very first time I contacted him three years ago, he welcomed me with open arms into the NUC-RIA group, and for that I am deeply thankful.

A very special acknowledgment goes to Manuel Xarepe, who in practice was my main mentor during this journey. His patience, availability, and constant willingness to teach made an invaluable difference. I learned immensely from him, and I can only hope that, upon reading this completed thesis, he will finally say to me: "good job".

I would also like to warmly thank the entire R^3B collaboration for the opportunities to learn and grow, and for immediately making me feel part of the team. I am especially grateful to Valerii Panin, spokesperson of the experiment, for proving that one can be both the smartest and the coolest person in the room at the same time. I would also like to give a special mention to Michael Heil, for his guidance on ToFD; to Prof. Dr. Meytal Duer, for making my Erasmus+ mobility with TU Darmstadt possible; to my friend Beatriz, to my hermanos in Galicia and to Martin Poghosyan, for their support, insights and friendship.

My thanks also go to my faculty, FCT NOVA, and in particular to the Department of Physics. I gratefully acknowledge the Erasmus+ program, without which my mobility to GSI would not have been possible. I also wish to thank GSI, and in particular the Get_INvolved program, of which I was fortunate to be a part. Finally, I thank LIP for supporting my participation in the R^3B Collaboration Meeting in York, England.

Now, I also want to thank two great friends that GSI gave me. Hiroshi, for all the deep talks about general relativity, clocks, and Beethoven — somehow managing to make every hang-out a mini-lecture. And Frederik, for sharing not only his friendship but also his friends, and for making me feel like a true Darmstädter.

> *"Become what you are!"*
>
> — **Nietzsche**, Thus Spoke Zarathustra
> (Philosopher)

Abstract

This thesis presents the development, simulation, and experimental application of reconstruction methods for light fragment detection using a Resistive Plate Chamber (RPC) in the framework of the R^3B collaboration at GSI. The work is carried out in the context of experiment G249, which investigates the structure of the neutron-rich nucleus ^{25}F via quasi-free scattering.

A central part of the thesis is the development of multidimensional fitting (MDF) functions within the R3BRoot framework, designed to reconstruct physical quantities from detector observables. Simulated datasets were used to train the MDF models with input from the FOOT tracking detectors, the GLAD dipole magnet, and the RPC. Functions were validated in Geant4-based simulations, achieving high predictive accuracy with uncertainties down to 10^{-3}, demonstrating robustness under realistic detector resolutions.

Simulations were also performed to estimate the fragment composition reaching the RPC, identifying deuterons, tritons, and alpha particles as dominant contributions.

The RPC performance during the G249 beam time was evaluated. Key results include a time resolution of 38 ps, efficiency of ~93% close to expectations, and identification of problematic strips affecting calibration. Preliminary applications of the MDF method to real data showed promising results for p/Q but poorer resolution for A/Q, attributed to ongoing detector calibration.

Overall, this work highlights the RPC's potential to evolve from a proton and timing detector to an active fragment reconstruction device, extending its role within R^3B and at FAIR.

Keywords: Resistive Plate Chamber (RPC), Quasi-free scattering (QFS), Multidimensional fitting (MDF), Exotic nuclei, R^3B collaboration

Resumo

Esta dissertação apresenta o desenvolvimento, simulação e aplicação experimental de métodos de reconstrução para a deteção de fragmentos leves utilizando uma Câmara de Placas Resistivas (RPC), no âmbito da colaboração R^{3}B no GSI. O trabalho é realizado no contexto da experiência G249, que investiga a estrutura do núcleo rico em neutrões ^{25}F através de reações em regime de dispersão quase-livre.

Uma parte central é o desenvolvimento de funções de ajuste multidimensional (MDF) no R3BRoot, concebidas para reconstruir grandezas físicas a partir de observáveis dos detetores. Conjuntos de dados simulados foram usados para treinar os modelos MDF com informação proveniente dos detetores FOOT, do dipolo GLAD e da RPC. As funções foram validadas em simulações baseadas no Geant4, atingindo elevada precisão preditiva com incertezas da ordem de 10^{-3}, demonstrando robustez em condições realistas.

Simulações adicionais estimaram a composição de fragmentos que atingem a RPC, identificando deutérios, trítios e partículas alfa como dominantes.

O desempenho da RPC durante o tempo de feixe da experiência G249 foi avaliado. Resultados principais incluem uma resolução temporal de 38 ps, eficiência de ~93% próxima das expectativas e a identificação de tiras problemáticas. As aplicações preliminares do método MDF a dados reais mostraram bons resultados para p/Q mas desempenho inferior para A/Q, atribuído à calibração ainda em curso.

Este trabalho evidencia o potencial da RPC em evoluir de um detetor de protões e tempo para um dispositivo ativo de reconstrução de fragmentos, ampliando o seu papel na R^{3}B e na FAIR.

Palavras-chave: Câmara de Placas Resistivas (RPC), Dispersão quase-livre (QFS), Ajuste multidimensional (MDF), Núcleos exóticos, Colaboração R^{3}B

CONTENTS

LIST OF FIGURES

Acronyms

<div align="right">

1

</div>

Introduction

> "The important thing in science is
> not so much to obtain new facts
> as to discover new ways of
> thinking about them."
>
> ———————————————
> Sir William Lawrence Bragg

Since the birth of Nuclear Physics, with the discovery of the atomic nucleus by Ernest Rutherford in 1911 [2], this area has proved to be a fascinating field for scientific research displaying a rich variety of quantum phenomena. Many of the exhibited features of the nucleons in the nucleus are similar to the structure and behavior of atomic electrons in the atom. Similar descriptions for energy levels and shells, spins and angular momentum have emerged.

But there are some differences:

1. The dominating force inside the nucleus is the strong force rather than the electromagnetic one.

2. Since the strong force is short range and attractive, the potential in which the nucleons exist is created by all the other nucleons in contrast to the force between the atomic electrons and the spatially separated positive charge of the nucleus [3].

Two fundamental models—the liquid-drop model [4] and the shell model [5]—represent key milestones in the development of understanding the nucleus. Their reconciliation explains many nuclear phenomena, particularly the emergence of magic numbers and the behavior of exotic nuclei.

1.1   The Liquid-drop Model

The liquid-drop model, first formulated comprehensively by Weizsäcker [6] and discussed in detail by Bethe and Bacher in 1936 [4], treats the nucleus analogously to a charged droplet

of incompressible fluid. This model emphasizes collective properties of the nucleus, such as binding energy, surface tension, and Coulomb repulsion among protons.

The semi-empirical mass formula (also called the Bethe-Weizsäcker formula) captures essential trends:

$$B(A, Z) = a_V A - a_S A^{2/3} - a_C \frac{Z(Z - 1)}{A^{1/3}} - a_A \frac{(N - Z)^2}{A} \pm \delta(N, Z)$$

where A is the mass number (total number of nucleons), Z is the proton number, and $N = A - Z$ is the neutron number. Each term accounts for volume (a_V), surface (a_S), Coulomb (a_C), asymmetry (a_A), and pairing (δ) effects respectively.

While successful at explaining global nuclear properties—such as the approximate binding energy per nucleon—it could not account for observed anomalies in nuclear stability, such as nuclei at specific nucleon numbers (2, 8, 20, 28, 50, 82, 126) exhibiting enhanced stability: the magic numbers.

1.2   The Shell Model

The limitations of the liquid-drop model led to the proposal of the nuclear shell model, developed independently by Maria Goeppert Mayer [5] and by Haxel, Jensen, and Suess [7] in the late 1940s. Mayer and Jensen later collaborated on a comprehensive treatment of the model [8], and were jointly awarded the Nobel Prize in Physics in 1963 for their contributions. Their work, expanding on the early suggestions of Elsasser [9], showed that nucleons move in quantized energy levels within a mean potential well created by all other nucleons—analogous to electrons in atomic orbitals.

Initially, it was thought that a simple three-dimensional harmonic oscillator potential could describe the structure. However, it was soon realized that including a strong spin-orbit coupling term, where the nucleon's spin couples to its orbital motion, was critical to reproduce the magic numbers observed experimentally [10].

In particular, spin-orbit splitting lifts the degeneracy of orbital states, energetically favoring high-angular-momentum states (e.g., $j = l + 1/2$), thus producing large energy gaps at specific nucleon numbers—those corresponding to the magic numbers. This effect is illustrated in Figure 1.1, which shows the rearrangement of single-particle levels and the resulting magic numbers emerging from spin-orbit coupling [11].

The modified energy level filling, based on this strong spin-orbit interaction, led to a successful explanation for the pronounced nuclear stability at nucleon numbers:

$$2, 8, 20, 28, 50, 82, 126$$

for both protons and neutrons separately [10].
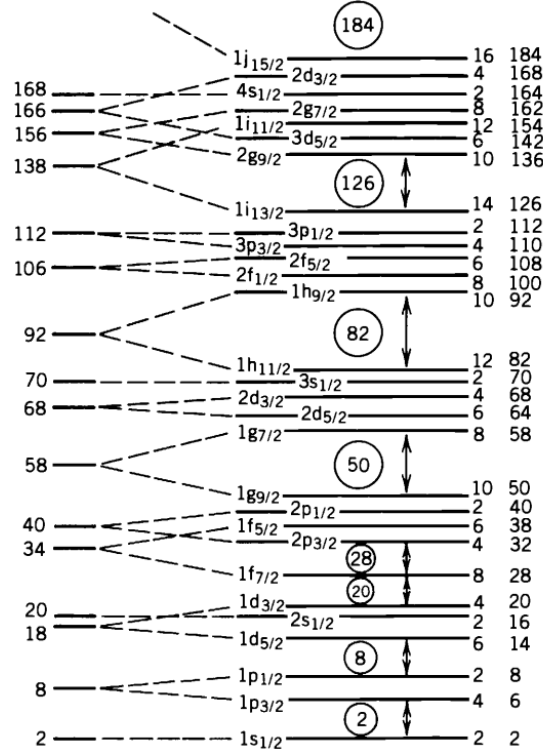
Figure 1.1: Single-particle shell model level scheme illustrating the origin of nuclear magic numbers after incorporating spin-orbit coupling. The diagram shows the energy splitting of nuclear orbitals due to spin-orbit interaction, leading to the observed magic numbers (circled) corresponding to closed shells at nucleon numbers 2, 8, 20, 28, 50, 82, 126, and 184. The levels are labeled with their orbital and total angular momentum quantum numbers *nlj*, and the associated degeneracy (2*j*+1) is indicated on the right. Reprinted figure from Ref. [11]

1.2.1 Magic Numbers and Shell Closures

In the shell model, a closed shell means that all available states at a given energy are filled. Nuclei with both proton and neutron numbers equal to magic numbers (so-called doubly magic nuclei, e.g., ^{16}O, ^{208}Pb) exhibit especially high binding energies, spherical shapes, and relatively low excitation spectra. Haxel, Jensen, and Suess [7] provided a succinct explanation showing how a strong spin-orbit coupling splits the energy levels such that filling up the states naturally reproduces the magic numbers.

1.2.2 Extension to Exotic Nuclei

The classic shell model was originally built based on stable and near-β-stable nuclei. However, advances in experimental techniques have allowed the study of exotic nuclei—nuclei far from stability, with unusual neutron-to-proton ratios.

In these systems traditional magic numbers can weaken or even disappear, new magic numbers (e.g., $N = 16$, $N = 34$) can emerge, nuclear deformations become more common, especially near the so-called "island of inversion" (around $N = 20$) and phenomena like

neutron halos emerge [12].

This phenomena has led to the concept of shell evolution, where the shell structure depends on the balance between the nuclear force components (central, spin-orbit, and tensor interactions) and changes with proton-neutron ratios.

In summary, the liquid-drop model offered a macroscopic view of nuclear behavior, while the shell model introduced microscopic structure and quantization effects that explain nuclear stability at magic numbers. The discovery of exotic nuclei has highlighted that the shell structure itself is dynamic and evolves under extreme conditions, demonstrating the richness and complexity of nuclear structure beyond the stable valley.

The quest for obtaining a model that will adequately describe the nucleus in all areas of stability, as well as at the extremes of nuclear existence has been motivating the last 60 years of nuclear physics and has led to the designing of new laboratories, such as the FAIR facility.

1.3   The FAIR Facility

The Facility for Antiproton and Ion Research (FAIR), currently under construction as an expansion to the existing GSI[1] in Darmstadt, Germany, represents one of the most ambitious research infrastructures worldwide for exploring the structure of matter and the evolution of the universe [13]. FAIR will provide intense, high-quality beams of protons, antiprotons, and ions—ranging from hydrogen to uranium—enabling unique access to a wide range of unexplored regimes in hadronic, nuclear, atomic, and plasma physics, as well as interdisciplinary and applied sciences.

The FAIR accelerator complex, seen in Figure 1.2, is centered around the superconducting synchrotron SIS100 [14], which, with its 100 Tm magnetic rigidity and 1100 m circumference, will serve as the backbone for beam delivery. The accelerator system is complemented by specialized storage rings and the Super-FRS fragment separator [15], facilitating the production and manipulation of both stable and exotic radioactive beams with intensities and purities that exceed those of existing facilities by several orders of magnitude.

FAIR's scientific program is structured around four foundational experimental pillars [13, 16, 17]:

- APPA – Atomic Physics, Plasma Physics, and Applications [18]

  The APPA collaboration focuses on high-precision studies in atomic and plasma physics, particularly utilizing highly charged ions and high-intensity ion beams. This enables research into correlated electron dynamics under ultra-strong electromagnetic fields, tests of quantum electrodynamics (QED) in critical regimes, and

---

[1]GSI Helmholtzzentrum für Schwerionenforschung
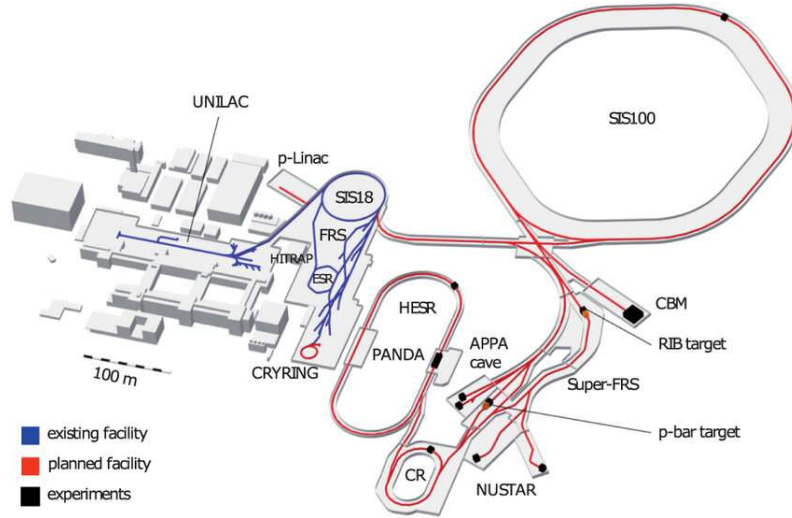
Figure 1.2: Layout of GSI-FAIR with the existing and planned beamlines shown in blue and red, respectively. The experimental sites are marked in black (figure: GSI Darmstadt). Reproduced from GSI-FAIR Website and Social Media Platforms. © Copyright: GSI/FAIR.

the investigation of high energy density matter relevant to astrophysical phenomena and fusion technologies. APPA also addresses applied sciences such as materials modification and radiation biology under cosmic-ray-like ion bombardment.

- CBM – Compressed Baryonic Matter [19]

  The CBM experiment aims to map the QCD phase diagram at high baryon densities and moderate temperatures, a region largely inaccessible to collider experiments like those at RHIC and LHC. Using high-intensity heavy-ion beams from SIS100, CBM will explore the properties of dense nuclear matter, the nuclear equation of state, and search for signals of deconfinement, chiral symmetry restoration, and the QCD critical point. It features the measurement of rare probes such as dileptons, open and hidden charm, and multi-strange hyperons with unprecedented statistics.

- PANDA – AntiProton ANnihilation at DArmstadt [20]

  PANDA will utilize antiproton beams stored and cooled in the High Energy Storage Ring (HESR) to investigate the structure of hadrons and their interactions. Its focus includes charmonium spectroscopy, the identification of exotic states such as hybrids and glueballs, and studies of the hadron mass generation mechanism via gluonic dynamics. PANDA's precision measurements are expected to yield insights into the strong force at the confinement scale, extending beyond the capabilities of previous antiproton experiments.

- NuSTAR – Nuclear Structure, Astrophysics, and Reactions [21]

  The NuSTAR collaboration (Nuclear Structure, Astrophysics and Reactions) lies at the heart of FAIR's mission to investigate nuclei far from stability and their relevance

in cosmic nucleosynthesis. NuSTAR's scientific objectives include exploring the structure of nuclei near the drip lines, understanding the processes driving the astrophysical r-process, and studying fundamental interactions and symmetries through decay modes and reaction dynamics of exotic nuclei.

Central to NuSTAR is the Super-FRS, a high-resolution, multi-stage fragment separator designed to deliver intense, isotope-pure beams of radioactive ions. These beams will allow exploration of previously inaccessible regions of the nuclear chart. A vital component of NuSTAR is the Reactions with Relativistic Radioactive Beams (R^3B) collaboration, which is dedicated to reaction studies in inverse kinematics using high-energy exotic nuclei. R^3B will enable kinematically complete measurements of a wide variety of reaction channels (e.g., knockout, breakup, Coulomb excitation), providing deep insights into nuclear forces, shell evolution, and exotic decay modes. The R^3B setup combines active and passive detectors in a versatile setup optimized for the coincident detection of charged particles, neutrons, and γ-rays.

1.4   Author's Contribution and Thesis Overview

The work presented in this thesis represents the author's direct contribution to both the simulation and analysis tasks within the framework of the R^3B collaboration, in the context of the G249 experiment. The author was responsible for developing and validating the multidimensional fitting (MDF) functions used to reconstruct physical quantities from detector observables. This involved designing the input variable set, training the models with simulated data, and evaluating their performance under realistic detector conditions. In addition, the author carried out dedicated simulations to estimate the particle distribution at the RPC, providing insight into the expected detector environment and potential additional physics channels relevant for G249.

This thesis is organized as follows. Chapter 2 introduces the theoretical and experimental background necessary to place the work in context. Chapter 3 describes the accelerator system at GSI and the R^3B experimental setup and its detectors, and further introduces the G249 experiment, outlining its goals, context, and beam characteristics. Chapter 4 is dedicated to the RPC, discussing its operating principles, construction, and relevance within R^3B. Chapter 5 presents the simulation studies, including the development and validation of the MDF approach. Finally, Chapter 6 discusses the experimental results, with a focus on the performance of the RPC as well as presenting preliminary applications of the MDF method to real data.

Direct Reactions as Spectroscopic Tools

"The art of simplicity is a puzzle
of complexity."

_____

Douglas Horton

The structure of atomic nuclei—how protons and neutrons arrange themselves in shells, how they correlate, and how these features evolve across the nuclear chart—has been at the heart of nuclear physics for decades [12]. To unravel this structure, nuclear physicists have long relied on direct reaction mechanisms, in which a projectile interacts with a target nucleus in a controlled and selective way, producing clean signatures of specific internal configurations [22]. Among these, transfer reactions and knockout reactions have historically provided the foundational experimental pathways for exploring the single-particle nature of the nucleus [22].

2.1 Transfer Reactions

Nucleon transfer reactions, such as (d,p), (p,d), or (t,α), involve the exchange of one or more nucleons between the projectile and the target [12, 23]. In the classic (d,p) reaction, for instance, a neutron is transferred from a deuteron to the target nucleus, leaving the residual system in a state that reveals the properties of the added neutron orbital [12].

These reactions have played a central role in defining the shell model: by measuring angular distributions and comparing them to reaction theory (e.g., using the distorted wave Born approximation, DWBA), one can extract:

- The orbital angular momentum l of the transferred nucleon (via angular distribution patterns) [12].

- The spectroscopic factor, quantifying the overlap between the initial and final nuclear states [12, 23].

Transfer reactions are best suited for stable or long-lived nuclei at relatively low energies (5–50 MeV/u), where they benefit from high cross-sections and well-developed theoretical

frameworks [24]. However, they become experimentally challenging for short-lived isotopes and high-Z systems, especially where targets cannot be fabricated [22].

2.2 Knockout Reactions

With the advent of radioactive beam facilities, transfer methods began to be complemented—and in some cases replaced—by nucleon knockout reactions, particularly in inverse kinematics [25]. In a knockout reaction, such as (A, A–1), a high-energy projectile nucleus collides with a light target (e.g., Be, C, or H), and a single nucleon is suddenly removed from the projectile [26].

Knockout reactions operate in the sudden approximation: the interaction is fast enough that the removed nucleon doesn't reconfigure its wavefunction during the process. The resulting residual nucleus and its kinematics encode the structural information of the pre-existing configuration [23, 25].

By measuring the momentum distribution of the residual fragment and comparing it with theoretical predictions (e.g., via the eikonal reaction model or Glauber theory), one obtains:

- The l-value of the knocked-out nucleon (from the width and shape of the distribution) [22, 25].

- The spectroscopic strength, linked to orbital occupancy [23, 25].

Knockout reactions revolutionized structure studies of exotic nuclei, especially those near the drip lines, by enabling measurements of systems that could only be formed in-flight [22, 23, 25].

2.3 From Knockout to Quasi-Free Scattering

While both transfer and knockout reactions have yielded profound insights, their selectivity and interpretability face limitations. Transfer reactions are constrained by target availability and are often restricted to stable systems [22]. Knockout reactions, although experimentally versatile, involve complex reaction dynamics with model dependencies that grow in neutron-rich environments and at higher energies [26, 27].

To transcend these limitations, quasi-free scattering has re-emerged as a uniquely powerful probe [25]. Conceptually close to knockout, but kinematically richer and theoretically cleaner in many regimes, quasi-free scattering reactions like (e,e′p) and (p,2p) offer direct access to the momentum and separation energy of individual nucleons in their initial nuclear orbitals [25, 28]. In high-energy kinematics, and under the impulse approximation, the scattering process isolates the interaction between the probe and a single nucleon, while the remaining nucleus acts as a spectator [25, 28].

This progression—from transfer, to knockout, to quasi-free scattering—represents not just an evolution of experimental technique, but a deepening of our ability to map the quantum landscape inside the nucleus, from its shell structure to the underlying many-body correlations [25].

2.4 Quasi-free Scattering Reactions

Quasi-free Scattering (QFS) has emerged as one of the most powerful tools in nuclear physics to probe the single-particle structure and correlations within atomic nuclei. It encompasses a class of reactions in which an incident probe (either an electron or a proton) interacts predominantly with a single nucleon in the nucleus, while the remaining nucleons act as passive spectators. Under kinematic conditions favoring large momentum and energy transfer, and small final-state interactions (FSI), the process can be approximated by the impulse approximation (IA)—a simplification in which the nuclear many-body system is treated as a collection of quasi-free, independent nucleons.

2.4.1 Historical Context and the Electron-Induced Paradigm

The conceptual and experimental foundations of QFS were established in the 1960s, particularly with the pioneering review by Jacob and Maris (1966) [29], which systematized the theoretical framework for electron-induced QFS reactions of the type (e,e′p). In these reactions, a high-energy electron transfers a well-defined amount of momentum and energy to a proton within the target nucleus, which is then ejected and detected in coincidence with the scattered electron. The kinematic constraints of such experiments enable the reconstruction of the missing energy and momentum of the ejected nucleon, which provides a direct spectroscopic window into the bound-state wavefunction.

This formalism was further refined in the 1973 follow-up by the same authors [30], which accounted for distortions in both the incoming and outgoing waves due to the nuclear potential—introducing the Distorted Wave Impulse Approximation (DWIA). These early (e,e′p) experiments, primarily conducted at SLAC and Saclay, provided critical benchmarks for understanding shell structure, spectroscopic factors, and occupancy probabilities, particularly in medium-mass nuclei like ^{16}O and ^{40}Ca. However, the method remained largely confined to stable nuclei due to the limitations in electron beam-target combinations.

2.4.2 Proton-Induced QFS and DWIA Evolution

In parallel, the use of proton-induced QFS—such as (p,2p) or (p,pn) reactions—gained traction as an alternative means to probe the same physics with hadronic probes [27]. While the complexity of the nucleon-nucleon (NN) interaction and stronger final-state interactions initially complicated the analysis, the development of DWIA for hadronic probes enabled the extraction of momentum distributions and spectroscopic observables
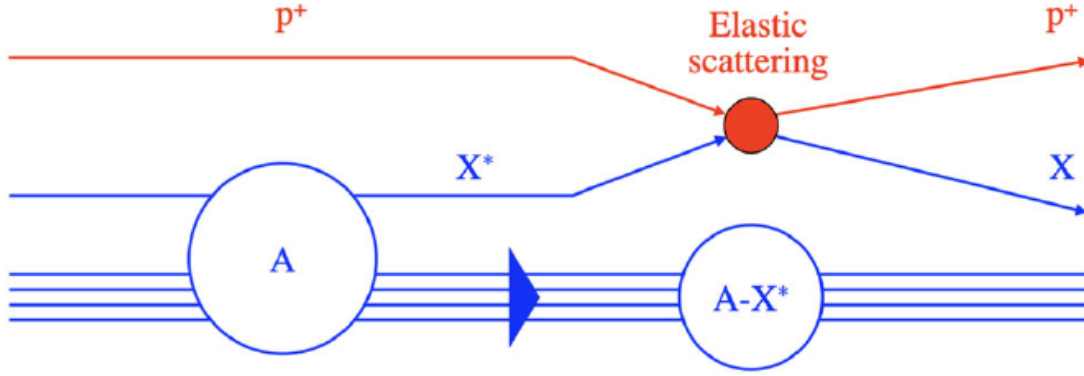
Figure 2.1: Schematic diagram of a QFS reaction induced by a proton p$^+$ on a nucleus A via elastic scattering off the virtual constituent particle X*. Three real particles are generated in the final state: the scattered proton p$^+$, the knock-out cluster X and the spectator nuclear fragment (A-X*). Reprinted figure from Ref. [25]

with comparable reliability. These reactions offered higher cross-sections and better experimental accessibility, though at the cost of increased theoretical uncertainty due to ambiguities in the NN scattering amplitude and optical potentials.

2.4.3 The Modern Era: Inverse Kinematics and Exotic Nuclei

A transformative leap occurred in the 21st century with the advent of inverse kinematics QFS using radioactive ion beams (RIBs) and hydrogen targets. As comprehensively reviewed by Panin et al. (2021) [25], modern QFS experiments at facilities such as RIKEN, GSI/FAIR, and FRIB utilize high-energy beams of neutron- or proton-rich nuclei impinging on proton-rich targets. The resulting reactions—such as (p,2p), (p,pn), or (p,pα)—enable the study of short-lived and exotic systems far from stability, including halo nuclei, nuclei near the neutron drip line, and those within the so-called "island of inversion."

These experiments exploit complete kinematic reconstruction techniques, coincident γ-ray detection, and high-resolution tracking of all final-state particles. This allows the identification of orbital angular momentum (l) of removed nucleons via momentum distributions, providing a model-independent probe of nuclear shell structure. Moreover, inverse kinematics QFS has facilitated the spectroscopy of unbound states, the quantification of short-range correlations (SRCs) [31–33], and insights into clustering phenomena in light and medium-mass nuclei [34–36].

2.4.4 Benchmark and Current Frontiers

QFS today occupies a unique position among reaction mechanisms, bridging single-particle and correlated many-body dynamics. Benchmarked by decades of electron-induced QFS data, modern (p, 2p)/(p, pn) measurements are now used to:

- Test shell evolution in neutron-rich isotopes.

- Quantify spectroscopic factors and their reduction (quenching).

- Investigate SRCs in asymmetric nuclear matter.

- Map the extent of the island of inversion.

- Explore the nature of unbound and resonant nuclear states.

Theoretical advancements, notably the eikonal DWIA and relativistic frameworks, allow consistent comparisons between experiment and shell-model or ab initio structure predictions. Future developments—such as the integration of machine learning in reaction theory, or the use of polarized beams and targets—promise even finer resolution of nuclear substructure.

Experimental Campaign G249 - ^{25}F Structure from QFS

> "Somewhere, something incredible is waiting to be known."
>
> Carl Sagan

3.1 Context and Goal of the Experiment

The proposed experiment, detailed in research proposal G-24-00249 [37], aims to investigate the structure of the neutron-rich fluorine isotope, ^{25}F, through one-proton knockout reactions. This study is motivated by the "drastic extension of the neutron drip line for Z=9 compared to Z=8 isotopes," a phenomenon that remains poorly understood [38]. The experiment seeks to elucidate how the ^{24}O core is polarized by the presence of an additional proton in ^{25}F, thereby shedding light on the mechanisms responsible for the observed drip line extension.

The experiment will employ the quasi-free scattering (QFS) reaction ^{25}F(p,2p)^{24}O in inverse kinematics, effectively knocking out a deeply bound valence proton from the ^{25}F nucleus [28]. This approach will utilize the R^{3}B experimental setup, including the high-efficiency neutron detector NeuLAND [39], to achieve complete kinematic measurements and obtain accurate spectroscopic information on the populated final states of ^{24}O. By analyzing the experimental data, researchers aim to determine the extent to which the single $d_{5/2}$ proton in ^{25}F modifies the structure of the core nucleons, potentially indicating deformation or polarization of the ^{24}O core [40].

Ultimately, the goal of this experiment is to provide a more detailed understanding of the nuclear structure of neutron-rich fluorine isotopes and the underlying reasons for the extended neutron drip line at Z=9. The results will contribute to a more comprehensive picture of nuclear forces and structure in exotic nuclei, addressing a fundamental question in nuclear physics.
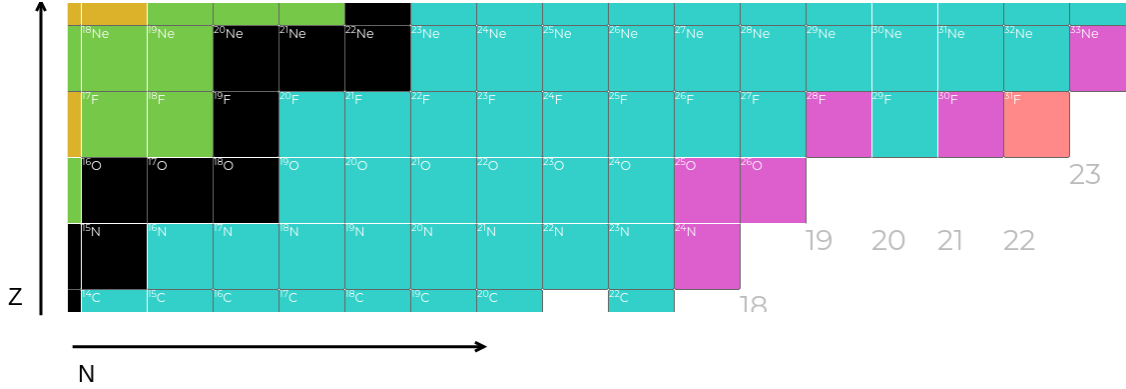
Figure 3.1: Visualization of the neutron drip line extension from oxygen, which is bound only up to ^{24}O, to fluorine, which remains bound up to ^{31}F. The extended neutron-rich limit for fluorine isotopes illustrates how additional protons influence nuclear binding near the drip line. Figure adapted from the IAEA Live Chart of Nuclides [41].

3.2 The GSI Accelerator System

The previously described experiment will take place at the GSI Helmholtzzentrum für Schwerionenforschung in Darmstadt, Germany. GSI's accelerator complex, shown in Figure 3.2, provides the infrastructure required to produce and deliver rare isotope beams, such as ^{25}F, for inverse kinematics reactions. The R^{3}B setup, located in Cave C downstream of the FRS, enables complete kinematic reconstruction, making it well-suited for the spectroscopic investigation of exotic nuclei. The following sections outline the accelerator chain that delivers these beams—from ion production through the UNILAC and SIS18 to the FRS and the experimental area.

3.2.1 Ion Beam Production

The accelerator cycle begins with the production of ions in specialized ion sources. Depending on the experimental requirements, different types of sources are used, including electron cyclotron resonance (ECR) sources and Penning ion sources [43]. These generate high charge state ions by stripping electrons from atoms in a plasma environment. The produced ions are pre-accelerated and then injected into the linear accelerator for further acceleration.

3.2.2 The UNILAC

The Universal Linear Accelerator (UNILAC) [44] serves as the primary injector for the GSI accelerator chain. It accelerates ions to energies of several MeV/u before their injection into the synchrotron. Structurally, the UNILAC consists of several stages: a radio-frequency quadrupole (RFQ), an interdigital H-mode drift tube linac (IH-DTL), and a transfer line to the synchrotron SIS18 [45]. Over the years, substantial upgrades have been implemented to accommodate high-intensity beams and improve the beam quality
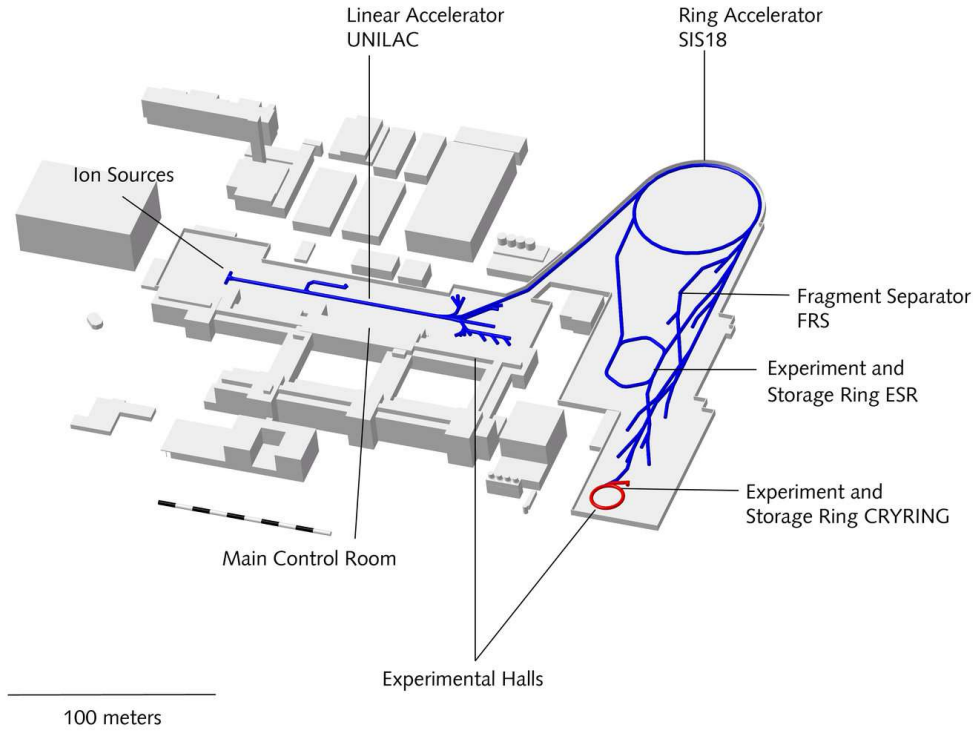
Figure 3.2: Schematic layout of the GSI Helmholtzzentrum accelerator facility. The diagram shows the major components including the ion sources, the UNILAC linear accelerator, the SIS18 synchrotron, the Fragment Separator (FRS), and the associated experimental halls [42].

for heavy ion acceleration . The layout of the UNILAC and its role as the front-end of the accelerator chain is depicted in Figure 3.3.

3.2.3 The SIS18 synchrotron

Following pre-acceleration by the UNILAC, ion beams are injected into the SIS18 synchrotron [46], where they are further accelerated to relativistic energies. The SIS18 is a fast-cycling synchrotron with a magnetic rigidity of up to 18 Tm, capable of accelerating ions to several hundred MeV/u. It incorporates sophisticated beam manipulation techniques including bunch compression and multiturn injection to optimize performance and beam delivery. Figure 3.4 illustrates the SIS18 layout and its specifications. The synchrotron serves both as a terminal accelerator for in-house experiments and as an injector for future FAIR components.

3.2.4 The Fragment Separator (FRS)

High-energy ions exiting the SIS18 are directed to the FRagment Separator (FRS) [48], a magnetic spectrometer designed for in-flight separation of rare isotopes. The FRS exploits differences in magnetic rigidity and energy loss to isolate specific nuclear species from a
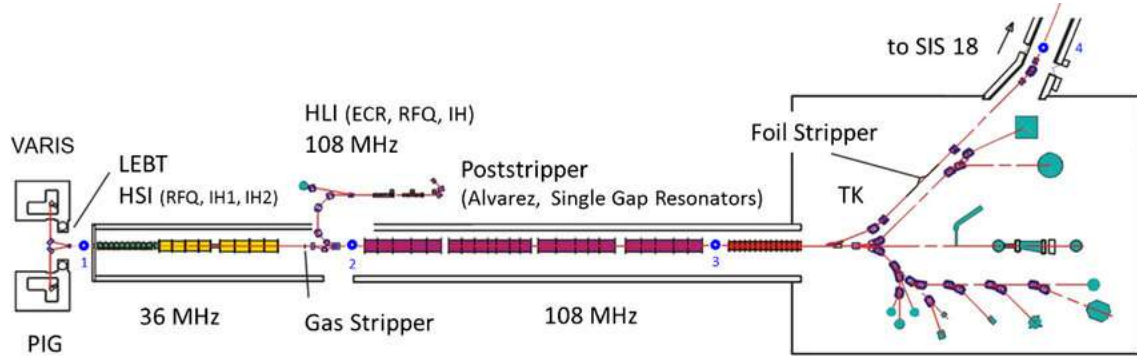
Figure 3.3: Detailed schematic of the UNILAC accelerator. The figure highlights the beamline structure from ion sources through the High Current Injector (HSI), Radio-Frequency Quadrupole (RFQ), Interdigital H-mode Drift Tube Linacs (IH-DTL), gas stripper section, Alvarez Drift Tube Linac (DTL), and the transfer line to SIS18. Beam diagnostic and stripping sections are also labeled [45].
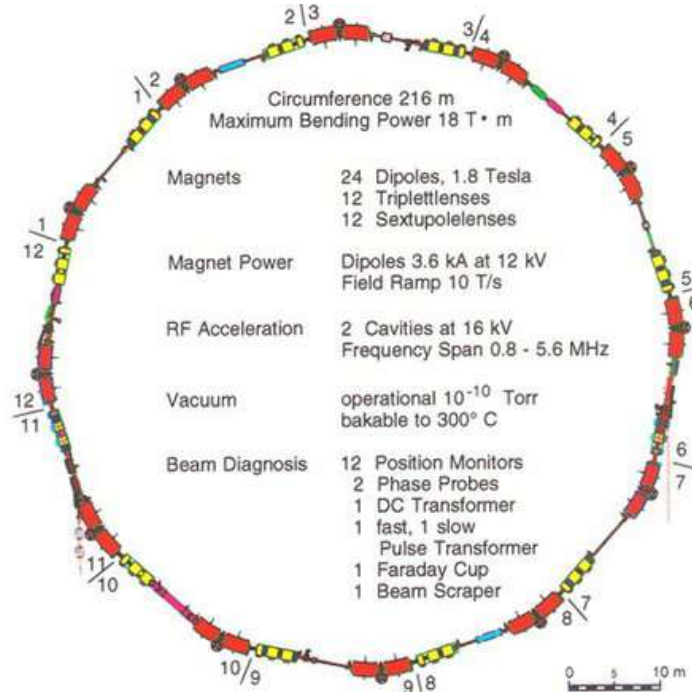
Figure 3.4: Plan view of the SIS18 heavy-ion synchrotron, illustrating its 12 identical lattice sections, dipole and quadrupole magnet configurations, RF acceleration cavities, and positions of beam diagnostic systems [47].

15
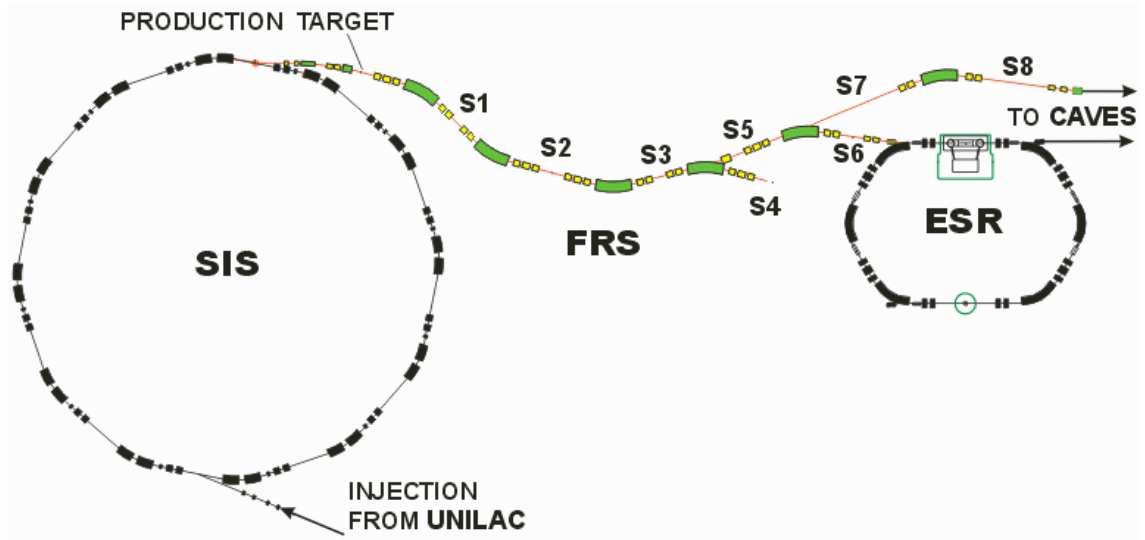
Figure 3.5: Schematic of the FRS system showing its dipole magnet sections, dispersive and achromatic focal planes (S1–S8), and the separation of rare isotope beams. The figure also shows the branching to dedicated experimental areas, including the Direct Branch, Ring Branch (ESR), and the experimental caves [49].

cocktail beam. It comprises four dipole magnets forming a two-stage separation system and includes focal planes for tracking, time-of-flight, and energy-loss measurements . As shown in Figure 3.5, the FRS facilitates beam transport from SIS18 to various experimental areas, enabling studies of exotic nuclei and reaction mechanisms.

3.2.5 Experimental Caves

Following separation in the FRS, ion beams are directed toward a suite of experimental stations, commonly referred to as experimental caves. These caves are equipped for diverse research programs ranging from nuclear structure and astrophysics to plasma physics and medical applications. One of the principal experimental areas is Cave C, located directly downstream of the FRS. This cave is the one that hosts the R^3B setup.

Cave C serves as a prototype environment for the future NUSTAR experiments at FAIR. Specifically, the R^3B instrumentation and experimental approach implemented at GSI are being used to develop and validate detector technologies and methodologies for the NUSTAR Cave under construction at FAIR. This strategic continuity ensures a seamless transition of experimental capabilities and scientific objectives from the current GSI facility to the FAIR complex.

The overall layout of the GSI accelerator chain and its future integration with FAIR, including the locations of Cave C and the planned NUSTAR cave, is illustrated in Figure 3.6.

The GSI accelerator system exemplifies a complex yet highly coordinated infrastructure, progressing from ion production through successive acceleration stages and culminating in precision experiments. The integration of the UNILAC, SIS18, and FRS ensures the
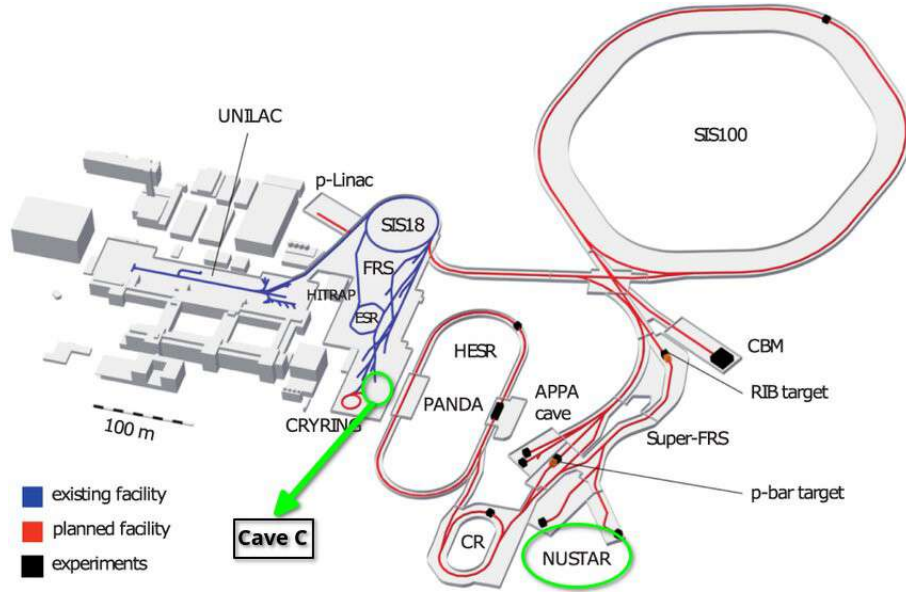
Figure 3.6: Layout of GSI-FAIR with Cave C highlighted, where the prototype of the future NUSTAR R^{3}B setup stands and where the experiment considered in this thesis took place.

delivery of high-intensity, high-quality ion beams, establishing GSI as a cornerstone of heavy ion research.

3.3 R^{3}B Setup

The R^{3}B (Reactions with Relativistic Radioactive Beams) setup at GSI is designed for high-precision, kinematically complete measurements of nuclear reactions involving rare isotope beams at relativistic energies. For the investigation of the ^{25}F(p,2p)^{24}O reaction, the configuration is optimized to detect all relevant particles emerging from the target—charged fragments, recoil protons, and neutrons—with high resolution and full angular coverage. The following description reflects the actual experimental layout, based on the schematic shown in Figure 3.7, and supported by the experimental proposal and detector-specific references.

17
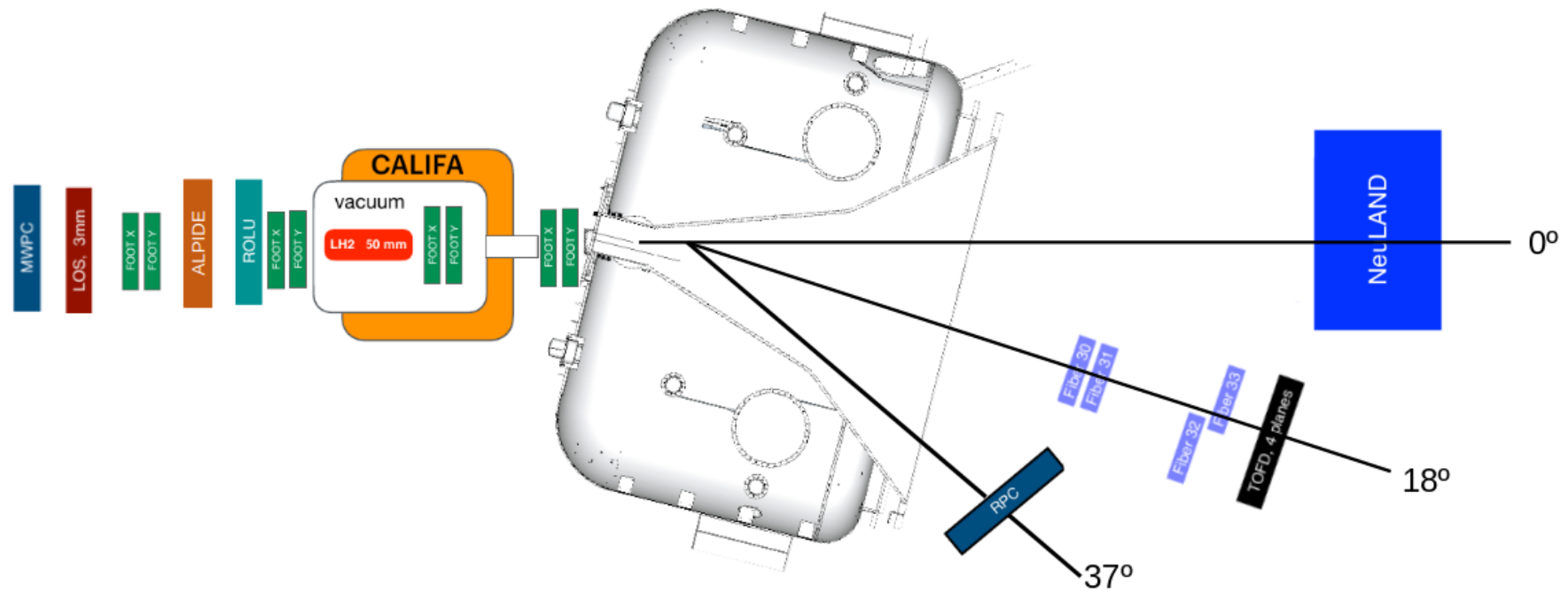
Figure 3.7: Sketch of the experimental setup at R^{3}B.

3.3.1 Beam Tracking and Initial Identification

At the end of the FRS, the experimental setup begins with a multi-wire proportional chamber (**MWPC**) placed at the entrance of Cave C. This detector provides coarse spatial information on the incoming secondary beam with minimal material interaction, supporting initial trajectory determination [50].

The **LOS** detector, positioned directly downstream of the MWPC, serves as the start detector for time-of-flight measurements and provides fast timing and energy-loss signals for particle identification. With a thickness of 3 mm, LOS offers good timing resolution while preserving beam quality [37].

Immediately following LOS, a pair of **FOOTs**—silicon-strip detectors—measure the position and energy loss of incoming ions. These detectors enable fine angular resolution and contribute to charge (Z) identification, enhancing particle-by-particle beam tagging.

3.3.2 ALPIDE: High-Precision Pixel Tracking

Downstream of the first FOOT pair, the beam encounters the **ALPIDE** detector. Originally developed for the ALICE ITS upgrade at CERN, ALPIDE is a monolithic active pixel sensor (MAPS) built using the 180 nm CMOS imaging process. Its architecture allows for in-pixel amplification and digitization with very low power consumption ($<40 \, \mathrm{mW/cm^2}$), high spatial resolution ($\sim 5 \, \mu\mathrm{m}$), and detection efficiencies exceeding 99% [51].

ALPIDE's design includes a fast, continuously active front-end and in-matrix sparsification, which minimizes data volume by transmitting only hit pixel addresses. This makes it ideal for high-rate tracking applications like R³B. Its placement directly before the target provides excellent vertex resolution when combined with upstream and downstream tracking data.

3.3.3 ROLU and Second FOOT Pair

The **ROLU** acts as a beam collimation device, though not in the form of a physical absorber. Instead, it consists of four plastic scintillators arranged to define a square aperture, with the individual scintillators movable to adjust the effective beam window. The system is integrated into the trigger logic: if a particle traverses one of the scintillators, a reject signal is issued and the corresponding event is discarded. Only particles passing cleanly through the defined square aperture—without activating the scintillators—are accepted as valid events. In this way, ROLU effectively performs the role of a beam collimator by suppressing halo particles and defining the accepted beam profile, while relying purely on veto logic rather than material absorption.

Immediately after ROLU is a second pair of FOOT detectors, which reinforces the pre-target tracking and ensures consistent charge and trajectory measurements across multiple stages.

3.3.4 Target and CALIFA

The nuclear reaction occurs in a 50 mm liquid hydrogen (LH$_2$) target, housed in a vacuum chamber and centrally located within the **CALIFA** (CALorimeter for In-Flight particles and γ-rays) detector. CALIFA is composed of CsI(Tl) crystals in a barrel geometry surrounding the target and is designed to detect both recoil protons and γ-rays emitted from excited nuclei. Its energy resolution ($\sim$5–6% at 1 MeV) and high granularity make it suitable for reconstructing angular distributions and reaction dynamics [52].

3.3.5 Post-Target Fragment Tracking

Two additional FOOT pairs are placed downstream of the target: one immediately following the exit window and the other just beyond CALIFA. These silicon-strip detectors provide post-reaction trajectory and Z information for the heavy charged fragments, supporting full momentum reconstruction and enabling vertex association when correlated with upstream tracks.

3.3.6 Magnetic Spectrometer: GLAD

The deflection of charged fragments is performed by **GLAD** (GSI Large Acceptance Dipole), a superconducting dipole magnet optimized for large-aperture, high-rigidity measurements. Operated at reduced current for this experiment, GLAD enables separation of oxygen isotopes by their magnetic rigidity, facilitating identification of the reaction residues such as ^{22}O, ^{23}O and ^{24}O.

3.3.7 Downstream Branches

After GLAD, the detection branches diverge to accommodate different particle species according to their magnetic rigidity:

- Neutron Arm: Neutrons produced in the decay of unbound states travel undeviated to **NeuLAND**, a high-efficiency detector composed of 3000 plastic scintillator bars. NeuLAND offers sub-150 ps time resolution and spatial precision of $\sim$1.5 cm, allowing for accurate time-of-flight measurements and invariant-mass reconstruction in multi-neutron events. It plays a central role in identifying final states like $^{23}O + n$ and $^{22}O + 2n$.

- Fragment Arm: Charged fragments deflected by GLAD are tracked by four **scintillating fiber detectors**, designated Fiber 30, 31, 32 and 33. These detectors provide fine spatial resolution along the beam axis. Final time-of-flight and charge identification are performed by the **Time-of-Flight Detector (ToFD)**, a four-plane plastic scintillator wall with timing precision better than 20 ps and Z resolution sufficient for fragment identification [53].

- Low Magnetic Rigidity Fragment Arm: A **Resistive Plate Chamber (RPC)** is also located in a separate branch downstream of GLAD. While its role in this experiment is limited to specific measurements, the RPC provides complementary timing and tracking information. A more detailed discussion of the RPC system will follow in the next chapter.

3.3.8 Main DAQ

The R^3B experimental setup is integrated through a centralized Data Acquisition (DAQ) system designed to operate in a trigger-coincidence mode across all detectors. Each detector is independently connected to the main DAQ and continuously monitors for signals corresponding to particle interactions. Upon detecting such a signal, a detector issues a trigger request to the central DAQ. When multiple detectors generate simultaneous or time-correlated trigger requests—indicative of a valid physical event—the system recognizes this as a global trigger. In response, the DAQ issues a trigger accept signal, prompting all participating detectors to read out and store the corresponding event data.

The digitized data from each detector are then merged into a single event stream and recorded in a common LMD (List Mode Data) file format. This format preserves the temporal correlation by organizing the information from all subsystems into event-by-event structures. To ensure consistency and temporal alignment across the detector systems, a synchronization signal is distributed at a frequency of approximately 10 Hz. This reference signal provides regular timing markers, allowing for verification and correction of potential timing drifts or misalignments during offline analysis.

3.4 Beam characteristics at G249

In the proposed experiment [37], a ^{40}Ar primary beam with an energy of 700 MeV/u is employed to produce a secondary beam containing the ^{25}F isotope of interest. The primary beam impinges on a beryllium target located at the FRS, inducing nuclear fragmentation reactions. This process generates a cocktail beam consisting of various isotopes, including ^{25}F at ~630 MeV/u, which is then selected and guided towards the experimental setup in Cave C.

The FRS is used to separate and purify the secondary beam, ensuring a sufficient intensity of ^{25}F for the subsequent experiment. As seen in Figure 3.8, LISE++ simulations, using the EPAX3.1a production model, predict an intensity of approximately 30 ions per second (pps) of ^{25}F on the secondary target [37]. The total intensity of the secondary cocktail beam in Cave C is expected to be below 700 pps, with a purity of around 5% for ^{25}F [37]. The relatively low total intensity allows for data acquisition without significant downscaling of triggers and minimizes dead time.

In Cave C, the ^{25}F secondary beam interacts with a liquid hydrogen (LH2) target, which serves as the reaction target for the one-proton knockout reaction ^{25}F(p,2p)^{24}O. The

^{24} Ne	^{25} Ne	^{26} Ne	^{27} Ne	^{28} Ne	^{29} Ne
		4.47e-1	3.19e+1	7.94e+0	2.57e-2
		0.003%	2.364%	8.192%	0.446%
^{23} F	^{24} F	^{25} F	^{26} F	^{27} F	
1.19e-1	4.12e+1	3.1e+1	2.86e-1	7.93e-6	
2e-4%	0.7%	6.879%	1.028%	5.6e-4%	
^{22} O	^{23} O	^{24} O			
1.04e+2	2.21e+0	5.14e-4			
4.561%	1.471%	0.006%			

Figure 3.8: Expected secondary cocktail beam of ^{25}F in Cave C as obtained by LISE++ calculations. The numbers under the names of isotopes indicate calculated rates per second. Reprinted figure from Ref. [37].

LH2 target is positioned in the center of the CALIFA calorimeter, enabling the detection of outgoing protons from the reaction. The use of a 150 mm thick LH2 cell was initially planned but, due to problems in the liquefaction phase, the cell was replaced for a 50 mm one, reducing the reaction yield.

3.5   Personal Contribution to the Experiment

Beyond the simulation and analysis work presented later in this thesis (with simulations described in Chapter 5 and analysis in Chapters 5 and 6), the author was actively involved in the experimental campaign. A key contribution was made to the preparation of the ToFD detector, ensuring its readiness for the experiment. Furthermore, the author played an important role during the beam time itself, taking regular shifts dedicated to the monitoring and operation of the RPC. This hands-on involvement provided valuable experience with the practical aspects of detector operation, complementing the simulation-based contributions presented in the subsequent chapters.

Resistive Plate Chambers

"The scientist is not a person who
gives the right answers, but one
who asks the right questions —
and builds the tools to answer
them."

Claude Lévi-Strauss
(paraphrased)

4.1 Introduction and Historical Context

Resistive Plate Chambers (RPCs) are gaseous ionization detectors introduced in the early 1980s by R. Santonico and R. Cardarelli [54] as a cost-effective solution for large-area charged-particle detection with excellent time resolution. Their working principle relies on the formation of localized electron avalanches in a thin gas gap between two resistive electrodes, typically made of glass or bakelite, under a strong uniform electric field [55]. When a charged particle traverses the gas volume, it ionizes the medium, creating primary electron-ion pairs. The applied electric field accelerates the liberated electrons, initiating an avalanche multiplication process that induces a fast signal on metallic readout strips placed outside the resistive electrodes.

The original single-gap RPC design offered sub-nanosecond timing capabilities and good detection efficiency at relatively low cost, making it widely adopted in high-energy physics experiments. Subsequent developments led to the introduction of Multi-Gap Resistive Plate Chambers (MRPCs), which consist of several narrow gas gaps arranged in parallel between resistive plates [55]. This configuration enhances the detector's timing precision by reducing statistical fluctuations in avalanche development and limiting the overall charge per avalanche, improving rate capability and stability. MRPCs have become the standard in modern time-of-flight (TOF) systems in nuclear and particle physics, delivering intrinsic time resolutions below 50 ps for minimum ionizing particles (MIPs) and efficiencies exceeding 98% [56].

Due to their scalability, robustness, and excellent timing performance, RPCs and MRPCs are extensively employed in experiments at facilities such as CERN, GSI, and RHIC, particularly in large TOF walls and tracking systems. Their application in relativistic heavy-ion collisions, rare-isotope beam experiments, and cosmic-ray detectors demonstrates their versatility and importance in modern experimental physics.

4.2 Detector Design, Construction, and Properties

The Resistive Plate Chamber (RPC) implemented in the R^3B experimental setup at GSI is a large-area timing detector developed for precise identification of charged fragments in relativistic heavy-ion collisions [56]. It is based on the Multi-Gap RPC (MRPC) concept, which significantly enhances timing performance through multiple narrow gas gaps that ensure stable avalanche development.

The detector comprises two identical modules, each hosting a six-gap glass stack, giving a total of twelve 0.3 mm-thick gas gaps per detection plane. These gaps are defined by nylon mono-filaments to guarantee uniform separation between the electrodes. The electrodes themselves consist of 1 mm-thick float glass coated with a resistive layer that provides uniform high-voltage distribution. Together, the modules form an active detection area of 1550×1250 mm^2 (1.94 m^2).

The readout system is composed of 41 copper strips, each 29 mm wide and 1600 mm long, arranged on a central PCB placed between the two modules. Each strip is read out on both ends, referred to as the left and right sides. This configuration enables reconstruction of the Y-position from the strip index and the X-position from the signal arrival time difference between both ends. Timing measurements are performed using front-end electronics based on the TRB3 (TDC Readout Board) [57] system developed at GSI, which provide fast leading-edge discrimination and time-over-threshold (ToT) encoding. TRB3 boards are equipped with multi-channel TDCs featuring sub-30 ps resolution, ensuring precise timing measurements even under high-rate conditions.

The detector operates in avalanche mode with a gas mixture of 98% tetrafluoroethane ($C_2H_2F_4$) and 2% sulfur hexafluoride (SF_6), maintained slightly below atmospheric pressure. The working voltage is approximately 8 kV per resistive plate, resulting in a total applied potential of ~16 kV per module. This configuration ensures efficient avalanche formation while suppressing streamer transitions and electrical breakdown.

Performance benchmarks obtained in previous tests and beam time campaigns confirm the excellent capabilities of this RPC design. The detector achieves a timing resolution of 50–80 ps for minimum ionizing particles in controlled conditions, and approximately 80–100 ps in realistic beam environments, where additional contributions from reference detectors and beam spread are included. The detection efficiency exceeds 95% under beam conditions and can reach 98% in optimized laboratory setups. Spatial resolution is governed by the 29 mm strip pitch in the vertical direction and the signal propagation
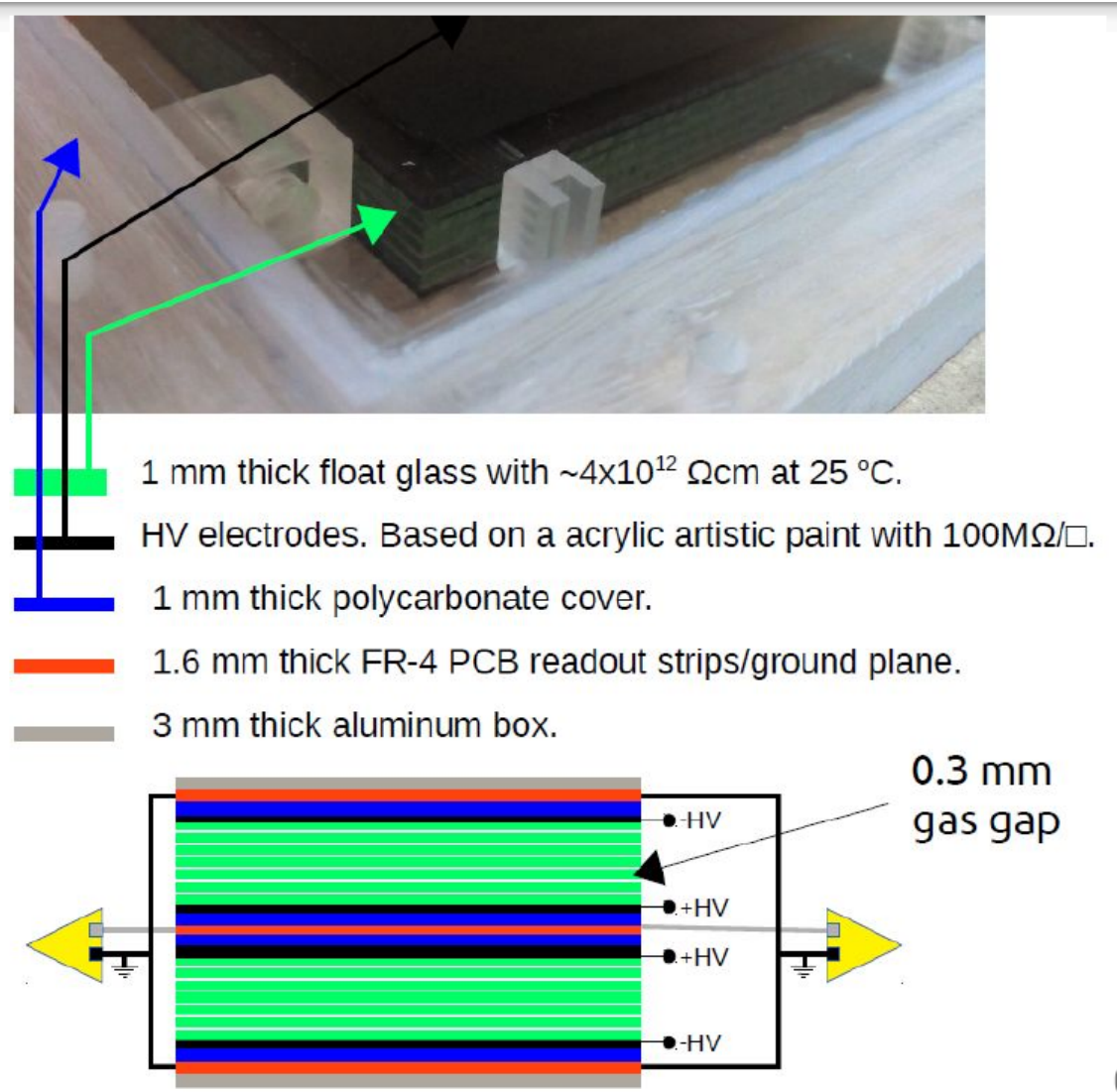
Figure 4.1: Schematic representation of the top view of the RPC. Reprinted from [56].

velocity along the strip for the horizontal position, yielding sub-centimeter accuracy in X after calibration [56, 58].

A schematic representation of the detector geometry and strip layout is shown in Figure 4.1.

4.3 Operating Principle and Gas System

4.3.1 Gas Mixture and Physics Motivation

The RPC operates with a carefully selected gas mixture composed of 98% tetrafluoroethane ($C_2H_2F_4$), also known as R-134a or Freon, and 2% sulfur hexafluoride (SF_6). This specific combination plays a critical role in establishing a stable and efficient ionization environment, ensuring optimal charge amplification and suppression of undesired discharges.

$C_2H_2F_4$ (Tetrafluoroethane)

As the primary component of the mixture, $C_2H_2F_4$ serves as the ionization medium and is responsible for supporting electron avalanches. Charged particles traversing the detector ionize the gas, liberating electrons that are accelerated by the applied electric field. Due to its moderate ionization energy (~13.10 eV) [59], $C_2H_2F_4$ enables efficient impact ionization, resulting in the formation of localized electron avalanches. Its polyatomic molecular structure provides internal vibrational modes that help absorb excess energy, thus preventing the transition to streamer mode. Furthermore, its relatively low electron diffusivity promotes spatially confined signal generation, preserving time resolution and detector stability.

SF_6 (Sulfur Hexafluoride)

Although present in a small fraction, SF_6 is vital to the safe operation of the RPC. As a strongly electronegative gas, SF_6 captures free electrons and suppresses excessive avalanche growth, thus preventing transitions to streamer or breakdown regimes. It also serves as a quenching agent by absorbing ultraviolet photons emitted by excited $C_2H_2F_4$ molecules, which would otherwise induce secondary avalanches. Through these mechanisms, SF_6 enhances the stability of the avalanche mode and significantly improves timing performance.

4.3.2 Operating Pressure

The internal pressure of the RPC is maintained slightly below atmospheric levels. This configuration is mechanically advantageous, as the higher external atmospheric pressure effectively compresses the detector structure, keeping the glass stacks firmly aligned and minimizing the risk of internal gaps or misalignments.

4.3.3 Detector Operating Modes

The RPC can, in principle, operate in three distinct regimes:

- Avalanche Mode (Preferred): The detector operates with controlled charge multiplication, producing fast, localized signals with minimal dead time. The presence of SF_6 is crucial to maintaining operation in this regime.

- Streamer Mode (Undesired): Inadequate quenching may lead to excessive avalanche growth and transition to streamer discharges, degrading time and spatial resolution and risking damage to the detector.

- Breakdown Mode (Failure): In the absence of sufficient suppression mechanisms, an uncontrolled discharge may occur, leading to continuous current flow and permanent damage to the detector plates.

The selected gas mixture and voltage operating point are tuned specifically to maintain operation within the avalanche mode, maximizing performance and longevity.

4.4 Readout Electronics and Signal Reconstruction

The RPC detector is read out using a differential system in which each of the signal strips is instrumented on both ends—referred to as the left and right sides. For each event in which a signal crosses a predefined threshold, the readout system records the strip number, the leading and trailing edge times (i.e., the time when the signal crosses the threshold on both the rising and falling edges), and the side (left or right) on which the signal was detected.

From this raw information, a hit can be reconstructed by extracting three key physical quantities: the spatial coordinates of the hit on the detector plane (X and Y), and the time information necessary for further analysis and event building.

- Y-position: The vertical position of the hit is determined directly from the strip number. Each strip has a fixed pitch (in this case, 3 cm), so the position along the Y-axis is given by the centerline of the corresponding strip.

- X-position: The horizontal position along the strip is reconstructed using the time difference between the left and right sides. Assuming a known signal propagation speed along the strip, the hit position is computed from the time asymmetry:

$$X = \frac{1}{2}(t_{right} - t_{left})$$

where t_{right} and t_{left} are the leading edge times on each end. This method assumes uniform propagation speed and symmetric signal shape, which are validated through calibration.

- Time Over Threshold (ToT): The time over threshold is defined as the difference between the trailing and leading edge times for a given signal. It provides an estimate of the pulse height (i.e., deposited charge) and is used as a quality criterion to discriminate valid hits from noise. Only signals with a ToT value within an expected range are accepted for further reconstruction.

This digital processing chain—from raw timing and strip information to physically meaningful hit coordinates—is integrated into the R^{3}B data processing framework. It enables high-resolution tracking and time measurement, critical for associating RPC hits with particle trajectories and for synchronization with the rest of the R^{3}B detector systems.

4.5 Performance in Test Beam Time prior to G249

The RPC system underwent its first test during beam time at the R^{3}B setup and demonstrated excellent performance. As seen in Figure 4.2, the detector achieved an efficiency
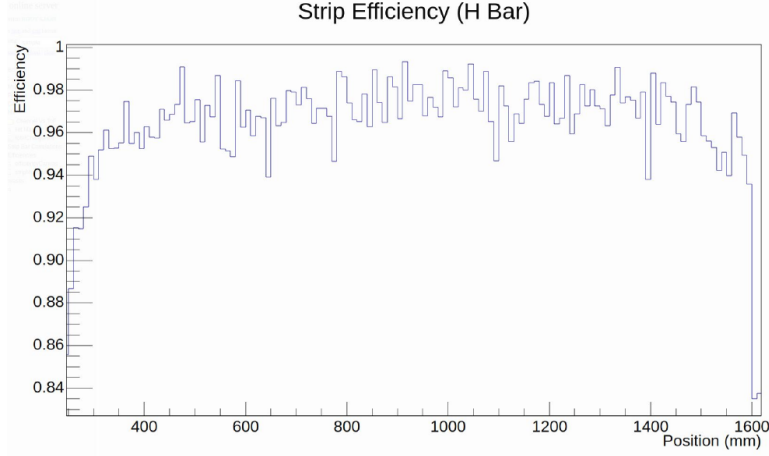
Figure 4.2: Measured strip efficiency of the RPC detector during the test beam time. Figure adapted from a presentation by M. Xarepe (personal communication, 2025).

exceeding 95%, with reliable synchronization with the rest of the R^3B detectors. The data acquisition was stable over the full two-week operation period, confirming the robustness of both the hardware and software components [58].

4.6 Role of the RPC in the Present Experiment

In previous implementations within the R^3B experimental setup, the RPC was primarily employed for the detection and timing of protons, operating under well-controlled conditions with relatively low particle multiplicity. The present experiment introduces a new challenge for the detector: the need to process a broader variety of charged particles, including heavier fragments. This scenario represents an important step in validating the RPC technology for more complex experimental conditions, aligning with future applications in FAIR and NUSTAR.

The motivation behind testing the RPC under these conditions lies in assessing its efficiency, timing performance, and overall stability when exposed to an extended particle spectrum beyond protons. Such an evaluation is critical for determining the feasibility of using RPCs as precision timing detectors in high-intensity, high-multiplicity environments, particularly where versatility in particle identification is required.

4.7 Detector Preparation Procedure

The preparation of the RPC prior to beam time involves several carefully controlled steps to ensure proper gas composition, structural stability, and operational calibration:

1. Drying Phase: Before filling with the working gas mixture, the RPC is flushed for several days with SF_6 to remove residual moisture. As a more cost-effective

alternative, nitrogen was used for this purpose; however, care must be taken to avoid over-pressurization, which could damage the delicate glass structure.

2. Leak Testing: Prior to introducing the working gas mixture, the system is tested for leaks. This is done by filling the gas lines while keeping the mass flow controllers closed and monitoring for pressure drops after closing the gas bottles. During this phase, a minor leak was detected. To localize it, various segments of the gas line were isolated and tested independently. These checks did not reveal any leakage in the external tubing, suggesting that the source of the leak was likely located within the RPC chamber itself, or at one of the gas inlet or outlet ports. Despite this issue, the leak was sufficiently small that it did not affect the detector's performance during beam time and did not require immediate intervention.

3. Gas Insertion and Calibration: Once leak tightness is confirmed, the $98\% \, C_2H_2F_4 \, / \, 2\% \, SF_6$ gas mixture is introduced. To determine the optimal operating voltage, the detector is calibrated using cosmic ray coincidence measurements. For this purpose, a scintillator NeuLAND bar is placed vertically on each side of the RPC. Coincidences allow for the fine adjustment of the high voltage supply to identify the working point that maximizes timing resolution and detection efficiency. An example of these calibration results is presented in Figure 4.3, which illustrates the dependence of efficiency and signal characteristics on the applied high voltage.

The entire preparation process takes approximately two weeks, after which the detector is ready for integration into the experimental campaign.

4.8 Contributions to Detector Operation and Monitoring

As part of the preparatory and operational phases of the experiment, several tasks related to the control and monitoring of the RPC system were developed or improved. These contributions focused on increasing system reliability, enabling remote intervention, and enhancing real-time observability during the beam time.

4.8.1 Monitoring Infrastructure for RPC Voltage and Current

To ensure the stable and safe operation of the RPC, a custom monitoring script was developed to continuously track the voltage and current supplied to the detector's resistive plates. This script interfaces with the high-voltage power supply and records the measured parameters at regular intervals. The collected data is automatically transmitted to a Grafana-based visualization dashboard, providing real-time insights into the detector's electrical behavior. This tool proved essential for diagnosing fluctuations, identifying abnormal conditions during beam time, and maintaining long-term performance stability. These monitoring plots, generated during beam time, are shown in Figure 4.4, where
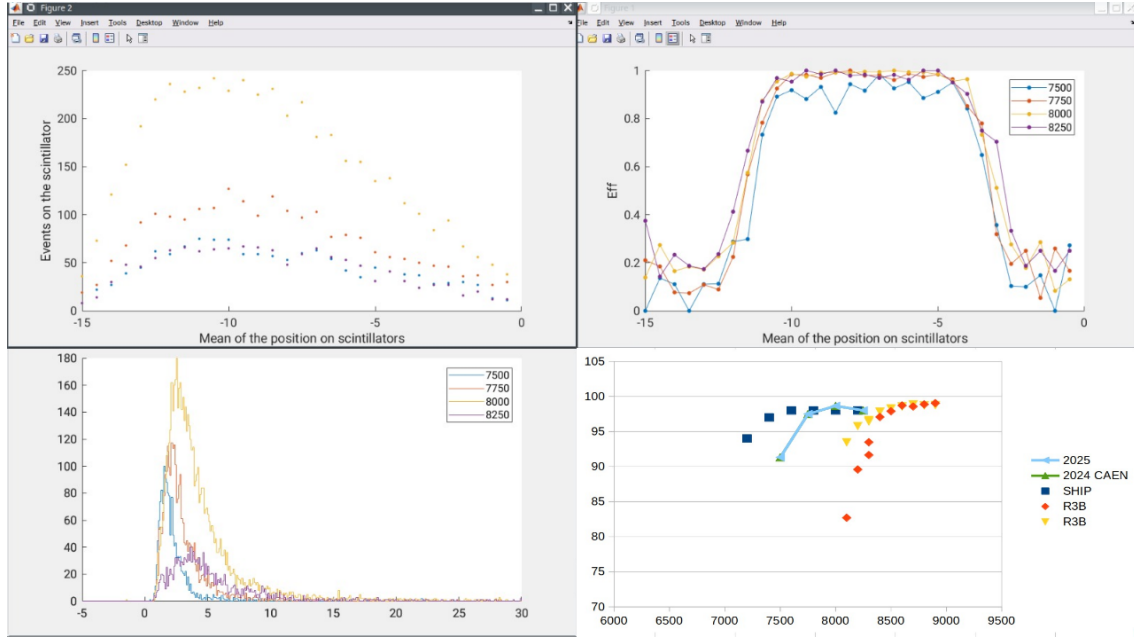
Figure 4.3: Calibration of the RPC working point using cosmic ray data. The top-left panel shows the distribution of events as a function of the mean position on the scintillators for different applied voltages. The top-right panel presents the corresponding efficiency curves as a function of position for four high-voltage settings (7500, 7750, 8000, and 8250 V). The bottom-left panel shows the time-over-threshold (ToT) distributions for the same voltages, which are used as a quality criterion for hit selection. The bottom-right panel summarizes the overall efficiency as a function of the applied voltage, including results from previous beam campaigns for comparison.

Figure 4.4: Example of live Grafana dashboard showing voltage and current monitoring of the RPC during beam operation.

the stability of the applied voltage and the corresponding current drawn by the resistive plates can be visualized over time.

4.8.2 Remote Control and Recovery Tools

In addition to monitoring, improvements were made to the RPC control interface by updating and correcting a script used for remote power cycling of the detector. This script also allows for the automated restart of the DAQ and acquisition systems, facilitating

rapid recovery in the event of software or hardware issues. These functionalities were used during beam time to reinitialize the RPC without requiring direct physical access to the electronics rack, minimizing downtime and ensuring uninterrupted data collection.

These tools contributed directly to the detector's robust operation and were successfully integrated into the experimental workflow.

SIMULATION AND ANALYSIS

> Whenever there is a problem, it
> usually lies between the chair and
> the monitor.
>
> ———————————
> M. Xarepe

Simulations are a fundamental component of modern nuclear physics experiments, providing a virtual environment where detector responses and physical processes can be modeled and tested prior to data acquisition. The work presented in this thesis was carried out using the R3BRoot framework, the dedicated simulation and analysis environment developed for experiments within the R^3B collaboration. Built upon the widely used Geant4 and ROOT packages, R3BRoot provides a comprehensive platform that combines accurate particle transport, flexible data handling, and experiment-specific detector models.
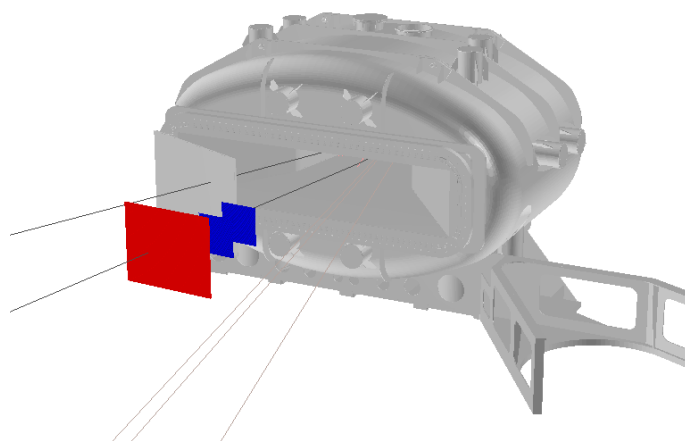
Figure 5.1: Example of an event in a simulation. In this case, there's a ^{14}C passing through ToFD, a Deuteron passing through the RPC and 3 neutrons going to NeuLAND.

5.1   Simulation and Analysis Frameworks

The simulations and analysis in this thesis were performed with R3BRoot [60], a framework specifically developed for the R^{3}B collaboration. It extends the FairRoot framework [61] and integrates two key tools in nuclear and high-energy physics: Geant4 [62] and ROOT [63].

Within this environment, Geant4 provides the physics engine for simulating the transport of particles through the experimental setup, accounting for interactions with detector materials, magnetic fields, and nuclear processes. This ensures that the modeled trajectories and energy losses accurately reflect the underlying physics.

ROOT serves as the backbone for data handling and analysis. It enables efficient storage of simulated events, statistical analysis, and visualization, as well as the application of reconstruction algorithms to large datasets.

By combining these elements, R3BRoot enables detailed end-to-end simulations of the ^{25}F(p,2p)^{24}O experiment. Particle generation, transport through the GLAD magnet and tracking detectors, and detection in the RPC were modeled with realistic detector resolutions and systematics. The resulting datasets not only replicate expected experimental conditions but also formed the basis for training and validating the multidimensional fitting (MDF) functions presented later in this chapter.

5.2   Simulation of Expected Fragments at the RPC

To evaluate the performance of the RPC and anticipate the type of particles reaching it during the experiment, dedicated simulations were performed using the R3BRoot framework. These simulations aimed to estimate the expected fragment distribution at the RPC detector and to assess the feasibility of studying additional physics channels beyond the primary reaction.

For this purpose, an INCL-generated event file corresponding to the reaction ^{22}O + p was used as input. While this is not the main reaction under investigation (^{25}F(p,2p)^{24}O), its inclusion is highly relevant since ^{22}O is predicted to be the dominant contaminant in the secondary beam, with an expected rate even higher than that of ^{25}F, as seen in Figure 3.8. Therefore, this simulation provides a realistic scenario for evaluating the RPC response under experimental conditions.

The geometry used for this study assumed floating detector volumes, meaning that the physical structures and electronics of the detectors were not included in the simulation. This simplification was chosen to accelerate the computation and focus on the kinematics of the fragments.

The primary observable analyzed was the correlation between the atomic number (Z) and the mass-to-charge ratio (A/Z) of the fragments arriving at the RPC, as shown in Figure 5.2. The results indicate that the most common fragments expected at the RPC are deuterons and alpha particles, and that an A/Z ratio of 2, dominates the distribution. This
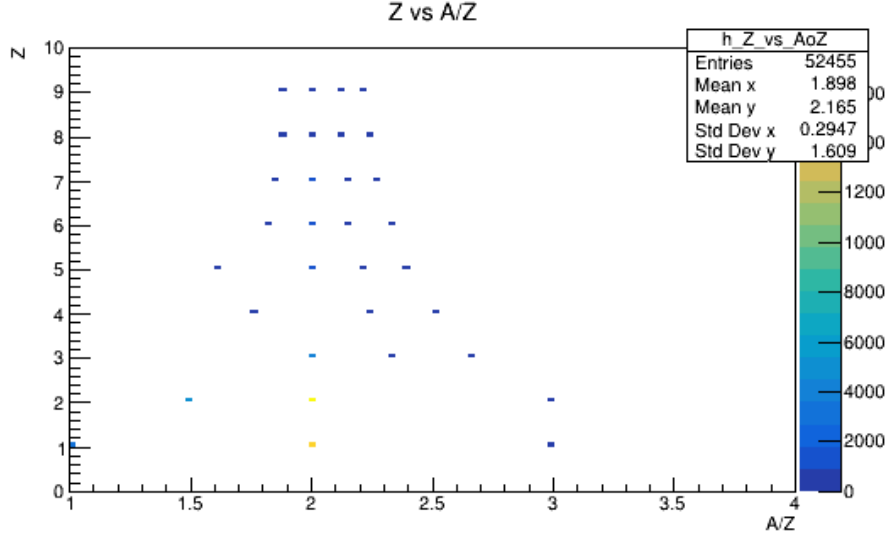
Figure 5.2: Distribution of fragments reaching the RPC, shown as a correlation between the atomic number (Z) and the mass-to-charge ratio (A/Z). The most common fragments are deuterons and alpha particles, with A/Z = 2 being the dominant region.

information is essential for defining reconstruction strategies and particle identification methods.

Furthermore, the simulation suggests that there may be opportunities to study additional reaction channels, such as (p,pα), during the experimental campaign, provided that sufficient statistics are collected for these events.

A more detailed discussion of these simulations, including additional plots and distributions of fragment properties, is presented in Appendix A.

5.3   Multidimensional Fitting

In experiments like those conducted with the R^{3}B setup, the information directly recorded by detectors is often insufficient on its own to fully reconstruct the physical quantities of interest. Raw observables such as hit positions and times must be interpreted in the context of the particle's full trajectory, charge, and energy. To bridge this gap, Multidimensional Fitting (MDF) methods, a procedure of the ROOT framework [64], are used. These tools allow us to model complex, nonlinear relationships between measurable detector signals and the underlying physical properties of particles.

Multidimensional fitting is particularly powerful in the context of quasi-free scattering reactions, such as the one studied in the ^{25}F(p,2p)^{24}O experiment. Given the diversity and overlap of signals produced by different particles and trajectories in the R^{3}B setup, MDF enables a more accurate reconstruction of particle kinematics by using correlated detector data. It also allows us to compensate for the intrinsic limitations of individual detectors by combining information from multiple systems.

5.3.1 Application to the RPC and FOOT Detectors

In the simulation phase of this work, MDF techniques were employed to enhance the reconstruction of particle kinematics at the RPC detector — the main focus of this thesis. To train the fitting models, a realistic dataset was generated by simulating the propagation of particles expected to be detected in the experiment, namely protons, alpha particles, deuterons, and ^{3}He nuclei. These particles were tracked from their production near the target, through the downstream tracking detectors (FOOTs), the GLAD magnet, and finally to the RPC.

Eight input variables were selected to capture the relevant kinematic and spatial information of the particles:

1. The x and y positions at the last pair of FOOT detectors;

2. The directional angles of the particles (Tx and Ty), calculated from the positions at both pairs of FOOTs downstream of the target;

3. The x, y and z positions at the RPC;

4. The time of flight between the last FOOT and the RPC.

These features encapsulate the spatial evolution and timing of particles along their flight path, providing the necessary information to infer more abstract physical quantities.

A MDF function to estimate the momentum over charge (p/Q) of particles was trained using this dataset.

Typically, in R^{3}B analyses, an additional MDF function is trained to estimate the flight path of the particle. When combined with the reconstructed momentum-over-charge (p/Q), this allows the calculation of the particle's velocity as a fraction of the speed of light (β) and the Lorentz factor (γ). These quantities are crucial for deriving the mass-to-charge ratio (A/Q), which plays an essential role in particle identification.

Initially, this approach was attempted in the present work by training a second MDF to predict the flight path from the same set of observables. However, the fitting procedure for this MDF did not converge properly and failed to provide a reliable minimization. This indicates that, given the chosen input variables, the correlation between the detector observables and the true flight path was not strong enough to allow for a robust fit.

To overcome this limitation, an alternative strategy was developed. Instead of estimating the flight path, a second MDF function was trained to predict the mass-to-charge ratio (A/Q) directly. For this purpose, the original eight input variables were used, and an additional ninth variable was introduced: the value of p/Q obtained from the first MDF. Including p/Q as an input significantly improved the predictive power of the second MDF, enabling it to infer A/Q with high accuracy.

The performance of this new approach was evaluated using a dedicated validation process (see Section 5.3.2), and the results were remarkably good. The differences between the predicted and true A/Q values were minimal, with uncertainties reaching the order

of 10^{-3} in normalized units. This demonstrates that the method is not only viable but also highly precise, making it a strong candidate for application in real experimental data analysis.

These trained models can later be applied to experimental data to infer momentum and trajectory parameters with higher confidence than would be possible using analytic approximations alone.

This approach demonstrates the importance of data-driven tools like MDF in modern nuclear physics experiments, where complexity and high dimensionality make traditional reconstruction methods insufficient.

5.3.2 Validation of the MDF Models

Once the MDF models were trained, their performance was validated using a new set of Geant4-based simulations that reproduced a realistic experimental scenario. These simulations included full beam-target reactions and accounted for detector resolution effects, ensuring that the generated observables reflected the uncertainties expected during actual data collection.

For each simulated event, the detector observables were extracted and used as input to the trained MDF functions, which reconstructed the physical parameters of interest. These reconstructed values were then compared with the known "true" values from the Geant4 simulations. The comparison was performed through a series of performance plots, with particular emphasis on the correlation between Q and A/Q. By contrasting the distributions obtained directly from the simulation with those reconstructed by the MDF functions, it was possible to visually and quantitatively assess the performance of the method (see Figures 5.3a and 5.3b).

5.4 Conclusions for the Experiment

Based on the preliminary simulations with the INCL model, the main fragments expected to reach the RPC are light ions, in particular deuterons and α particles. The results indicated that species with A/Q = 2 will dominate the detected distribution, reflecting the kinematic conditions and contaminant contributions from ^{22}O. This outcome is relevant not only to anticipate the particle environment at the RPC, but also to assess the feasibility of studying additional physics channels, such as (p,pα) reactions.

The results of the MDF method demonstrated excellent agreement between the reconstructed and simulated quantities. The residuals between predicted and true values were typically small, with uncertainties reaching down to the order of 10^{-3} in normalized units. This high level of precision confirms that the trained MDF functions are robust and reliable under realistic conditions.

These findings are significant for the role of the RPC detector within the R^{3}B setup. Traditionally, the RPC has been considered primarily as a timing and proton detector,

providing precise time-of-flight measurements for knocked out protons. However, the results of this study indicate that, in principle, the RPC could also serve as a fragment reconstruction detector, provided that the MDF method performs equally well when applied to real experimental data. This would increase the importance of the RPC within the current experimental framework and could extend its potential role in future facilities, such as the FAIR High Energy Cave, where enhanced fragment identification capabilities would be highly valuable.
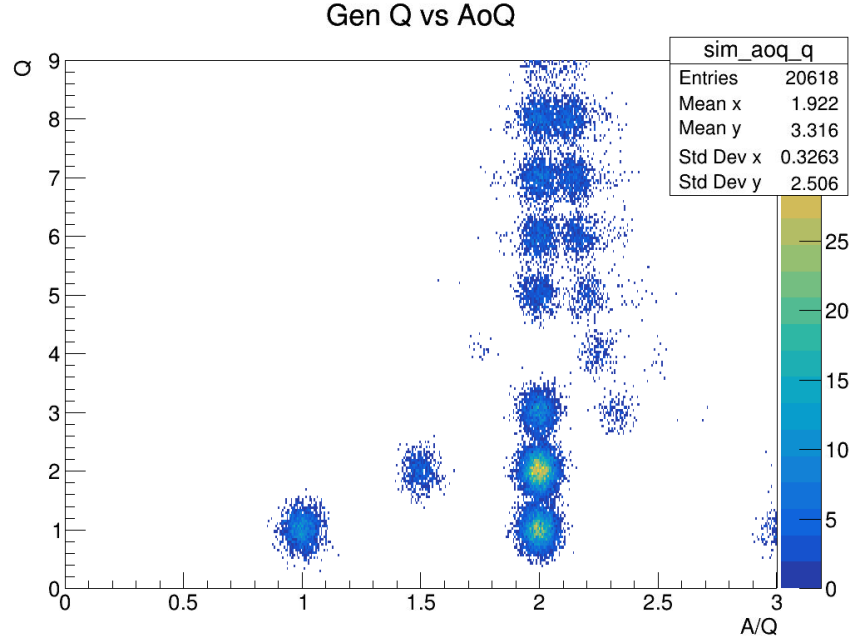
(a) Correlation between Q and A/Q obtained directly from Geant4 simulations, including detector resolution effects.
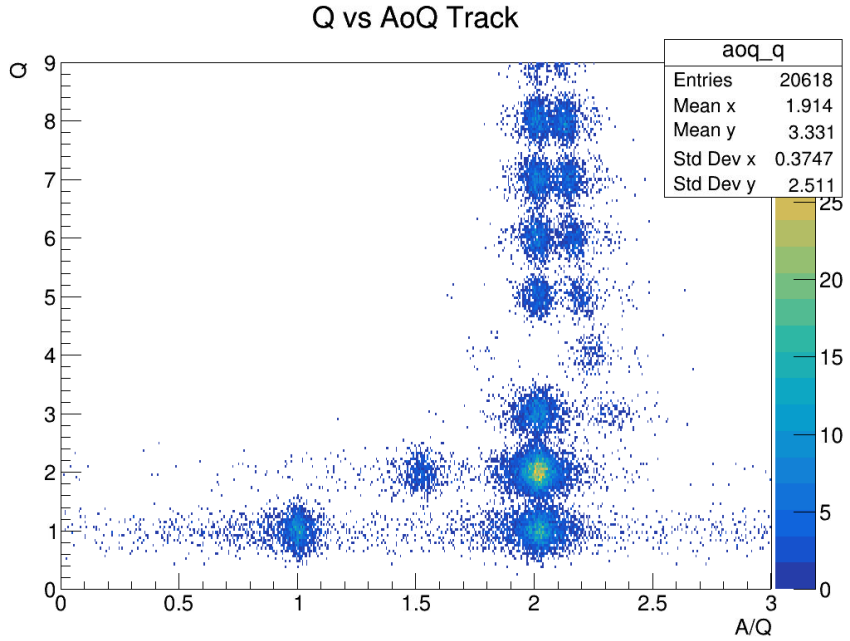
(b) Correlation between Q and A/Q reconstructed using the trained MDF functions.

Figure 5.3: Comparison between simulated (a) and MDF-reconstructed (b) correlations of charge Q and mass-to-charge ratio A/Q.

<div align="right">

6

</div>

<div align="right">

Results and Discussion

</div>

> In science, results are not the end, but the beginning of understanding.

6.1 Performance of the RPC During the Experiment

6.1.1 RPC Acceptance

An initial step in the analysis consisted in evaluating the performance of the RPC during the experiment and compare it to expectations from the simulation campaign. This validation was necessary to ensure the reliability of subsequent analyses relying on RPC data.

Figure 6.1 shows the hit map of the RPC obtained from real experimental data alongside the corresponding map from the simulations. The comparison confirms that the RPC acceptance during the experiment is consistent with the simulated expectations, providing confidence in the validity of the simulation framework for modeling RPC response.

6.1.2 Electronic Time Resolution

To assess the electronic time resolution of the detector system, a dedicated pulser test was performed by simultaneously pulsing the LOS detector and the RPC and measuring the time difference between the two signals. The resulting distribution, shown in Figure 6.2, yielded a Gaussian width of $\sigma = 38$ ps, which is in line with the performance observed in previous experiments and confirms the stability of the electronic chain.

6.1.3 Time-of-Flight Calibration

The time response of individual strips was further investigated by plotting the time-of-flight (ToF) as a function of the RPC strip number (Figure 6.3). While the majority of strips behaved as expected, several exhibited anomalous timing behavior, suggesting localized

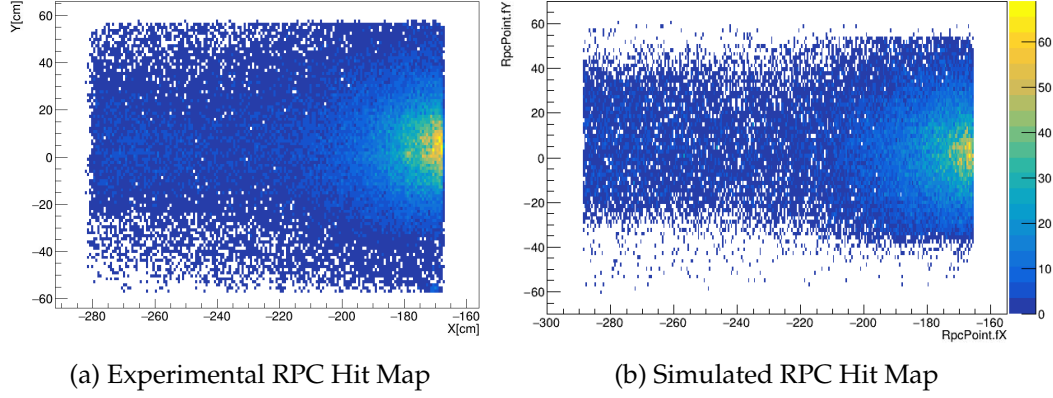(a) Experimental RPC Hit Map

(b) Simulated RPC Hit Map

Figure 6.1: Hit map of the RPC obtained from experimental data compared to simulations. The consistency in the acceptance region validates the simulation framework for modeling RPC response.
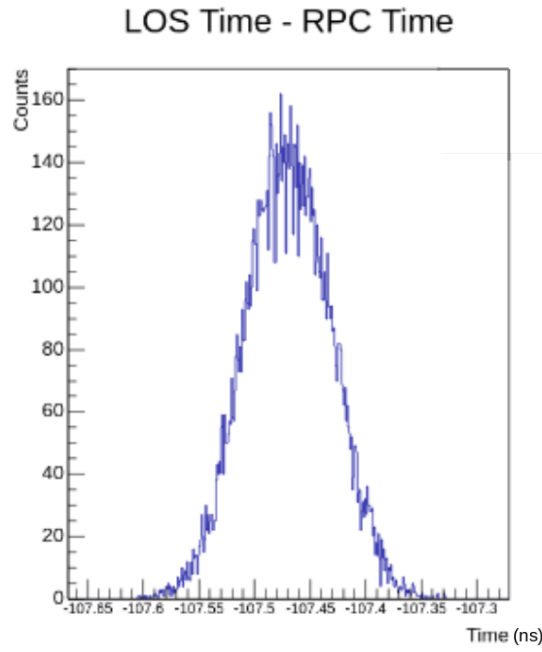

Figure 6.2: Distribution of the time difference between LOS and RPC signals obtained with a pulser test. The standard deviation of the distribution is $\sigma = 38$ ps, consistent with previous experimental results.
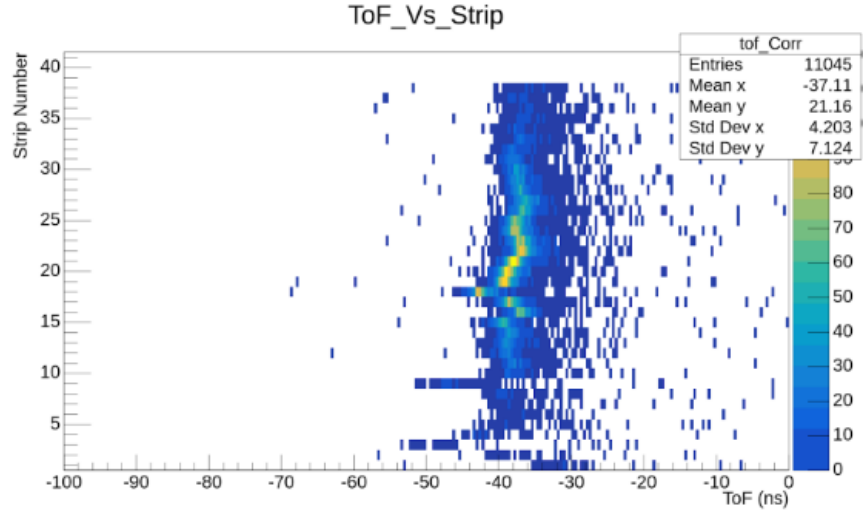
Figure 6.3: Time-of-flight as a function of the RPC strip number. Several strips show anomalous timing behavior, highlighting localized inefficiencies that require further calibration.

inefficiencies or calibration issues. This observation indicates that additional work will be required to properly account for these problematic strips, and it foreshadows challenges that will appear later in the analysis stage.

6.1.4 Efficiency

Finally, the overall efficiency of the RPC was evaluated and is presented in Figure 6.4. The measured efficiency, of around 93%, was found to be slightly below the levels achieved in previous experiments. This reduction can be attributed to the chosen operating conditions: while the nominal working point of the detector was 8250 V, during this experiment the high voltage applied to the resistive plates was deliberately set to 8000 V. This precautionary adjustment was taken to mitigate potential risks, given the lack of prior experience operating the RPC with heavier fragments. Although it reduced the overall efficiency, this choice was necessary to ensure detector safety under the experimental conditions.

6.2 MDF Method Application to Real Experimental Data

After validating the MDF models on simulated data, the next step was their application to real experimental events. To facilitate this analysis, an initial event selection strategy was implemented using the ToFD detector as a veto. By requiring the absence of a ToFD hit, it was possible to assume that the hits reconstructed in the FOOT detectors correspond directly to those reaching the RPC, thus avoiding the ambiguities associated with multi-hit scenarios.
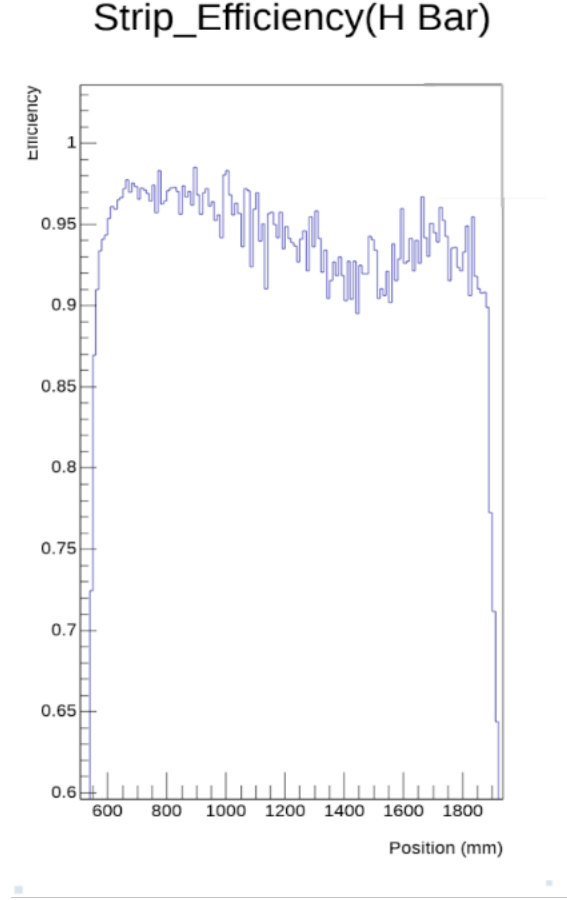
Figure 6.4: Overall RPC detection efficiency. The slightly reduced performance compared to previous experiments is attributed to the lower operating voltage applied to protect the detector when exposed to heavier fragments.

However, this approach introduces complications. A physical gap exists between the ToFD and the RPC, meaning that multi-fragment events can still occur where one fragment passes through the gap while another is detected in the RPC. Additionally, charge determination using FOOTs alone is subject to limitations: at low charges, the FOOT resolution does not allow a clean separation between species with charges 2 and 3. Despite these caveats, the veto condition provides a practical starting point for the analysis.

To refine the selection and mitigate multi-hit ambiguities, an extended method was developed by explicitly including ToFD information. When multiple FOOT hits are present, they are separated according to their reconstructed charges. The charge of the fragment reaching the RPC is then inferred by comparing with the charge measured in ToFD: if ToFD registers a high charge, the lower-charge FOOT hit is selected for the RPC, and vice versa. In cases where no ToFD hit is present, the FOOT charge assignment is retained. Furthermore, when a ToFD hit exists, the charge of the RPC fragment is estimated as the difference between the incoming beam charge (given by LOS) and the ToFD charge, assuming that the missing charge corresponds to the RPC fragment. For the
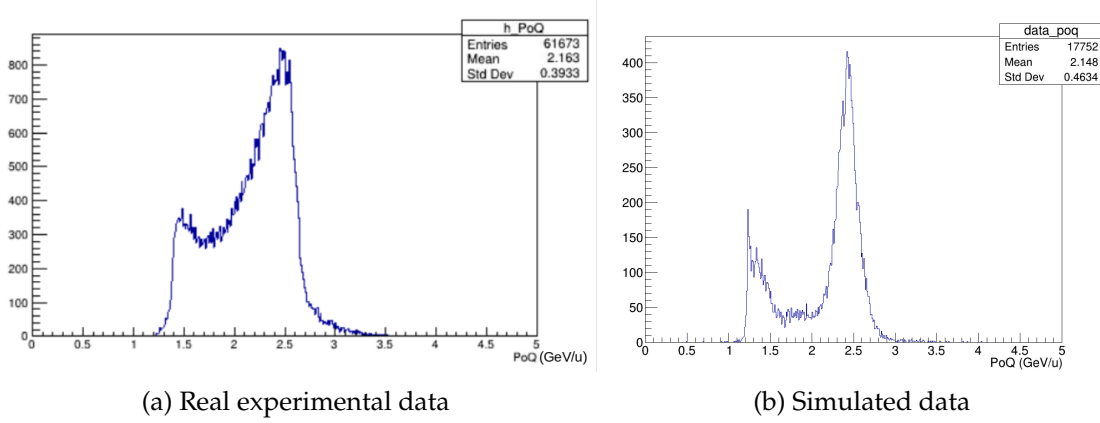
42

(a) Real experimental data

(b) Simulated data

Figure 6.5: Comparison of momentum-over-charge (p/Q) distributions reconstructed by the MDF. The close agreement between both diagrams highlights the consistency of the MDF performance across real and simulated conditions.
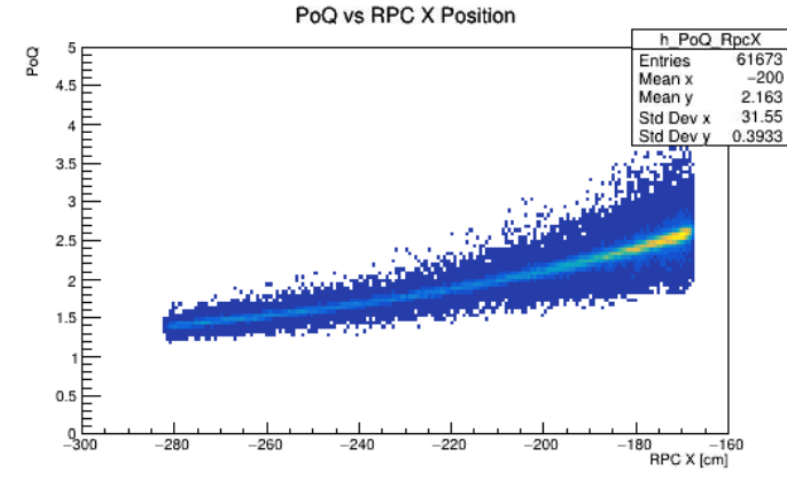

Figure 6.6: Correlation between RPC hit position in the x-coordinate and the reconstructed p/Q from real data. The expected curved dependence confirms the physical consistency of the MDF results for p/Q.

present analysis, events were selected with an incoming beam charge of 8 or 9 and with multiplicity one in the RPC.

The results of applying the MDF functions to real data show a mixed performance. The MDF trained to reconstruct p/Q yielded consistent results, in agreement with expectations from simulations. This is evident from the comparison of the p/Q distributions in real and simulated data (Figure 6.5) as well as from the correlation between the RPC hit position in the x-coordinate and the reconstructed p/Q, which follows the expected curve (Figure 6.6). In contrast, the MDF for A/Q did not perform as well. The reconstructed values exhibited a poor resolution and an unphysical tail toward zero, as shown in Figure 6.7. In the particle identification (PID) plots of A/Q versus Q (Figure 6.8), instead of well-separated blobs corresponding to different fragments, broad horizontal bands were observed due to the large dispersion in A/Q.

43
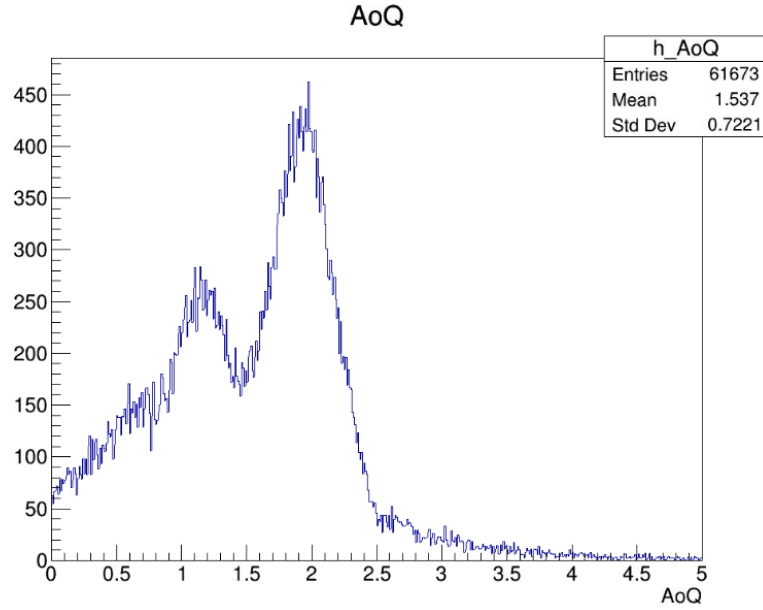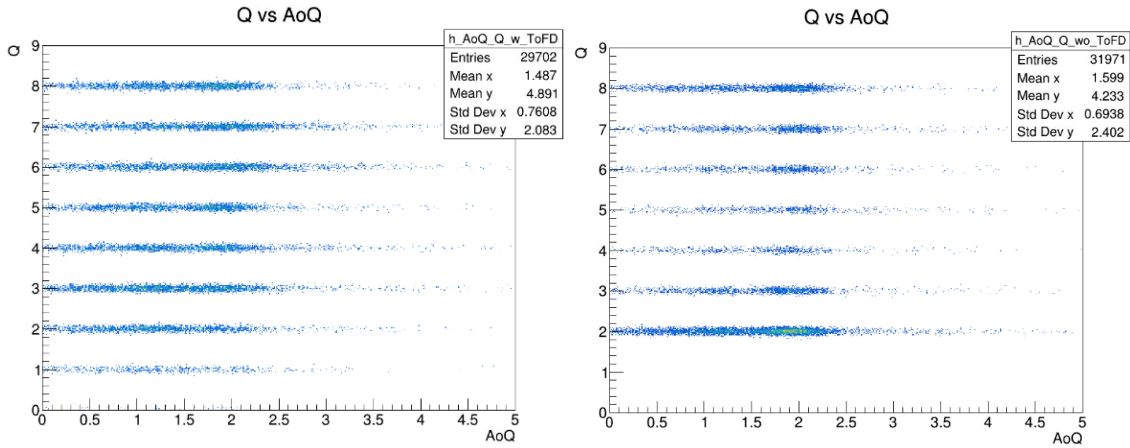
Figure 6.7: Distribution of mass-to-charge ratio (A/Q) reconstructed by the MDF from real experimental data. The broad dispersion and unphysical tail toward zero reflect the limitations of the current calibration stage.

(a) PID with ToFD

(b) PID without ToFD

Figure 6.8: Particle identification plots of A/Q versus charge Q reconstructed by the MDF. (a) Events selected with ToFD information. (b) Events selected without ToFD information. In both cases, instead of well-separated clusters, broad horizontal bands are observed, indicating poor A/Q resolution at this stage.

44

This behavior can be understood as a consequence of calibration limitations. At this stage, detector calibrations across the setup are still ongoing: while the RPC calibration is being refined by the author, the FOOT detectors are under calibration by other members of the collaboration. From the simulation studies presented in Chapter 5, it was shown that the MDF prediction of A/Q is highly sensitive to the time-of-flight (TOF) observable. Indeed, by artificially worsening the TOF resolution in simulations, similar patterns emerge to those observed in real data, with highly dispersed A/Q values and horizontal PID bands. This strongly suggests that the current limitations originate from an incomplete calibration of the RPC TOF response, as also evidenced earlier in the analysis of strip-dependent timing issues.

These findings highlight both the potential and the present challenges of applying MDF to real experimental data. While the p/Q reconstruction is already promising, the reliable extraction of A/Q requires further improvements in detector calibration and possibly a more refined event selection strategy.

6.3 Outlook and Future Work

The present analysis should be regarded as preliminary. Future work will focus on completing the calibration of all relevant detectors, with particular emphasis on improving the RPC time-of-flight determination. This step is expected to significantly enhance the MDF performance for A/Q and enable clearer fragment separation in the PID plots. Additionally, further refinement of the hit selection procedure in the FOOT detectors and more stringent charge assignment strategies will be explored to reduce multi-hit ambiguities.

Ultimately, achieving robust PID reconstruction with the MDF method would elevate the role of the RPC beyond its traditional use as a proton and timing detector. It would position the RPC as a versatile fragment detector, capable of contributing significantly to present R^{3}B experiments and future applications in the FAIR High Energy Cave.

Bibliography

[1] J. M. Lourenço. *The NOVAthesis LaTeX Template User's Manual*. NOVA University Lisbon. 2021. URL: https://github.com/joaomlourenco/novathesis/raw/main/template.pdf (cit. on p. i).

[2] E. Rutherford. "LXXIX. *The scattering of and particles by matter and the structure of the atom*". en. In: *The London, Edinburgh, and Dublin Philosophical Magazine and Journal of Science* 21.125 (1911-05), pp. 669–688. ISSN: 1941-5982, 1941-5990. DOI: 10.1080/14786440508637080. URL: https://www.tandfonline.com/doi/full/10.1080/14786440508637080 (cit. on p. 1).

[3] J. T. Taylor. "Proton induced quasi-free scattering with inverse kinematics". PhD thesis. University of Liverpool, 2011 (cit. on p. 1).

[4] H. A. Bethe and R. F. Bacher. "Nuclear Physics A. Stationary States of Nuclei". en. In: *Reviews of Modern Physics* 8.2 (1936-04), pp. 82–229. ISSN: 0034-6861. DOI: 10.1103/RevModPhys.8.82. URL: https://link.aps.org/doi/10.1103/RevModPhys.8.82 (cit. on p. 1).

[5] M. G. Mayer. "On Closed Shells in Nuclei". In: *Phys. Rev.* 74 (3 1948-08), pp. 235–239. DOI: 10.1103/PhysRev.74.235. URL: https://link.aps.org/doi/10.1103/PhysRev.74.235 (cit. on pp. 1, 2).

[6] C. F. von Weizsacker. "Zur Theorie der Kernmassen". de. In: *Eur. Phys. J. A* 96.7-8 (1935-07), pp. 431–458 (cit. on p. 1).

[7] O. Haxel and J. H. D. Jensen. "On the "Magic Numbers" in Nuclear Structure". en. In: () (cit. on pp. 2, 3).

[8] M. G. Mayer and J. H. D. Jensen. *Elementary Theory of Nuclear Shell Structure*. Wiley, 1955 (cit. on p. 2).

[9] W. M. Elsasser. "Sur le principe de Pauli dans les noyaux". fr. In: *Journal de Physique et le Radium* 4.10 (1933), pp. 549–556. ISSN: 0368-3842. DOI: 10.1051/jphysrad:01933004010054900. URL: http://www.edpsciences.org/10.1051/jphysrad:01933004010054900 (cit. on p. 2).

[10] M. G. Mayer, J. Hans, and D. Jensen. "SHELL CLOSURE AND jj COUPLING". en. In: *Alpha-, Beta- and Gamma-Ray Spectroscopy*. Elsevier, 1968, pp. 557–582. ISBN: 978-0-7204-0083-0. DOI: 10.1016/B978-0-7204-0083-0.50020-1. URL: https://linkinghub.elsevier.com/retrieve/pii/B9780720400830500201 (cit. on p. 2).

[11] K. S. Krane. *Introductory nuclear physics*. en. Rev. ed., [Nachdr.] Hoboken, NJ: Wiley, 1988. ISBN: 978-0-471-80553-3 (cit. on pp. 2, 3).

[12] T. Otsuka et al. "Evolution of shell structure in exotic nuclei". en. In: *Reviews of Modern Physics* 92.1 (2020-03), p. 015002. ISSN: 0034-6861, 1539-0756. DOI: 10.1103/RevModPhys.92.015002. URL: https://link.aps.org/doi/10.1103/RevModPhys.92.015002 (cit. on pp. 4, 7).

[13] H. Stoecker and C. Sturm. "The FAIR start". en. In: *Nuclear Physics A* 855.1 (2011-04), pp. 506–509. ISSN: 03759474. DOI: 10.1016/j.nuclphysa.2011.02.117. URL: https://linkinghub.elsevier.com/retrieve/pii/S0375947411002041 (cit. on p. 4).

[14] P. Spiller et al. "The FAIR Heavy Ion Synchrotron SIS100". en. In: *Journal of Instrumentation* 15.12 (2020-12), T12013–T12013. ISSN: 1748-0221. DOI: 10.1088/1748-0221/15/12/T12013. URL: https://iopscience.iop.org/article/10.1088/1748-0221/15/12/T12013 (cit. on p. 4).

[15] M. Winkler et al. "The status of the Super-FRS in-flight facility at FAIR". en. In: *Nuclear Instruments and Methods in Physics Research Section B: Beam Interactions with Materials and Atoms* 266.19-20 (2008-10), pp. 4183–4187. ISSN: 0168583X. DOI: 10.1016/j.nimb.2008.05.073. URL: https://linkinghub.elsevier.com/retrieve/pii/S0168583X08007015 (cit. on p. 4).

[16] C. Sturm, B. Sharkov, and H. Stöcker. "1, 2, 3 . . . FAIR !" en. In: *Nuclear Physics A* 834.1-4 (2010-03), pp. 682c–687c. ISSN: 03759474. DOI: 10.1016/j.nuclphysa.2010.01.124. URL: https://linkinghub.elsevier.com/retrieve/pii/S0375947410001259 (cit. on p. 4).

[17] G. Rosner. "Future Facility: FAIR at GSI". en. In: *Nuclear Physics B - Proceedings Supplements* 167 (2007-05), pp. 77–81. ISSN: 09205632. DOI: 10.1016/j.nuclphysbps.2006.12.089. URL: https://linkinghub.elsevier.com/retrieve/pii/S0920563206010516 (cit. on p. 4).

[18] T. Stöhlker et al. "APPA at FAIR: From fundamental to applied research". en. In: *Nuclear Instruments and Methods in Physics Research Section B: Beam Interactions with Materials and Atoms* 365 (2015-12), pp. 680–685. ISSN: 0168583X. DOI: 10.1016/j.nimb.2015.07.077. URL: https://linkinghub.elsevier.com/retrieve/pii/S0168583X15006552 (cit. on p. 4).

[19] K. Agarwal. "The Compressed Baryonic Matter (CBM) Experiment at FAIR – Physics, Status and Prospects". en. In: *Physica Scripta* (2023-02). ISSN: 0031-8949, 1402-4896. DOI: 10.1088/1402-4896/acbca7. URL: https://iopscience.iop.org/article/10.1088/1402-4896/acbca7 (cit. on p. 5).

[20] M. Destefanis. "The PANDA experiment at FAIR". en. In: *Nuclear Physics B - Proceedings Supplements* 245 (2013-12), pp. 199–206. ISSN: 09205632. DOI: 10.1016/j.nuclphysbps.2013.10.040. URL: https://linkinghub.elsevier.com/retrieve/pii/S0920563213006269 (cit. on p. 5).

[21] T. Nilsson and for the NUSTAR collaboration. "The NUSTAR project at FAIR". en. In: *Physica Scripta* T166 (2015-11), p. 014070. ISSN: 0031-8949, 1402-4896. DOI: 10.1088/0031-8949/2015/T166/014070. URL: https://iopscience.iop.org/article/10.1088/0031-8949/2015/T166/014070 (cit. on p. 5).

[22] R. F. Casten and B. M. Sherrill. "The study of exotic nuclei". In: *Progress in Particle and Nuclear Physics* 45 (2000), S171–S233. ISSN: 0146-6410. DOI: https://doi.org/10.1016/S0146-6410(00)90013-9. URL: https://www.sciencedirect.com/science/article/pii/S0146641000900139 (cit. on pp. 7, 8).

[23] A. Gade et al. "Reduction of spectroscopic strength: Weakly-bound and strongly-bound single-particle states studied using one-nucleon knockout reactions". en. In: *Physical Review C* 77.4 (2008-04), p. 044306. ISSN: 0556-2813, 1089-490X. DOI: 10.1103/PhysRevC.77.044306. URL: https://link.aps.org/doi/10.1103/PhysRevC.77.044306 (cit. on pp. 7, 8).

[24] G. R. Satchler. *Direct nuclear reactions*. 1983-01 (cit. on p. 8).

[25] V. Panin, T. Aumann, and C. A. Bertulani. "Quasi-free scattering in inverse kinematics as a tool to unveil the structure of nuclei: A tribute to Mahir S. Hussein". en. In: *The European Physical Journal A* 57.3 (2021-03), p. 103. ISSN: 1434-6001, 1434-601X. DOI: 10.1140/epja/s10050-021-00416-9. URL: https://link.springer.com/10.1140/epja/s10050-021-00416-9 (cit. on pp. 8–10).

[26] V. Panin et al. "Quasi-free proton knockout from 12C on carbon target at 398 MeV/u". en. In: *Physics Letters B* 797 (2019-10), p. 134802. ISSN: 03702693. DOI: 10.1016/j.physletb.2019.134802. URL: https://linkinghub.elsevier.com/retrieve/pii/S0370269319305064 (cit. on p. 8).

[27] T. Aumann, C. A. Bertulani, and J. Ryckebusch. "Quasifree (p , 2 p) and (p , p n) reactions with unstable nuclei". en. In: *Physical Review C* 88.6 (2013-12), p. 064610. ISSN: 0556-2813, 1089-490X. DOI: 10.1103/PhysRevC.88.064610. URL: https://link.aps.org/doi/10.1103/PhysRevC.88.064610 (cit. on pp. 8, 9).

[28] V. Panin et al. "Exclusive measurements of quasi-free proton scattering reactions in inverse and complete kinematics". en. In: *Physics Letters B* 753 (2016-02), pp. 204–210. ISSN: 03702693. DOI: `10.1016/j.physletb.2015.11.082`. URL: `https://linkinghub.elsevier.com/retrieve/pii/S0370269315009612` (cit. on pp. 8, 12).

[29] G. Jacob and T. A. J. Maris. "Quasi-Free Scattering and Nuclear Structure". en. In: *Reviews of Modern Physics* 38.1 (1966-01), pp. 121–142. ISSN: 0034-6861. DOI: `10.1103/RevModPhys.38.121`. URL: `https://link.aps.org/doi/10.1103/RevModPhys.38.121` (cit. on p. 9).

[30] G. Jacob and T. A. J. Maris. "Quasi-Free Scattering and Nuclear Structure. II." en. In: *Reviews of Modern Physics* 45.1 (1973-01), pp. 6–21. ISSN: 0034-6861. DOI: `10.1103/RevModPhys.45.6`. URL: `https://link.aps.org/doi/10.1103/RevModPhys.45.6` (cit. on p. 9).

[31] O. Hen et al. "Nucleon-nucleon correlations, short-lived excitations, and the quarks within". en. In: *Reviews of Modern Physics* 89.4 (2017-11), p. 045002. ISSN: 0034-6861, 1539-0756. DOI: `10.1103/RevModPhys.89.045002`. URL: `https://link.aps.org/doi/10.1103/RevModPhys.89.045002` (cit. on p. 10).

[32] M. Duer et al. "Direct Observation of Proton-Neutron Short-Range Correlation Dominance in Heavy Nuclei". en. In: *Physical Review Letters* 122.17 (2019-05), p. 172502. ISSN: 0031-9007, 1079-7114. DOI: `10.1103/PhysRevLett.122.172502`. URL: `https://link.aps.org/doi/10.1103/PhysRevLett.122.172502` (cit. on p. 10).

[33] A. Schmidt et al. "Probing the core of the strong nuclear interaction". en. In: *Nature* 578.7796 (2020-02), pp. 540–544. ISSN: 0028-0836, 1476-4687. DOI: `10.1038/s41586-020-2021-6`. URL: `https://www.nature.com/articles/s41586-020-2021-6` (cit. on p. 10).

[34] F. M. Marqués et al. "Detection of neutron clusters". en. In: *Physical Review C* 65.4 (2002-04), p. 044006. ISSN: 0556-2813, 1089-490X. DOI: `10.1103/PhysRevC.65.044006`. URL: `https://link.aps.org/doi/10.1103/PhysRevC.65.044006` (cit. on p. 10).

[35] F. M. Marqués and J. Carbonell. "The quest for light multineutron systems". en. In: *The European Physical Journal A* 57.3 (2021-03), p. 105. ISSN: 1434-6001, 1434-601X. DOI: `10.1140/epja/s10050-021-00417-8`. URL: `https://link.springer.com/10.1140/epja/s10050-021-00417-8` (cit. on p. 10).

[36] M. Duer et al. "Observation of a correlated free four-neutron system". en. In: *Nature* 606.7915 (2022-06), pp. 678–682. ISSN: 0028-0836, 1476-4687. DOI: `10.1038/s41586-022-04827-6`. URL: `https://www.nature.com/articles/s41586-022-04827-6` (cit. on p. 10).

[37] V. Panin et al. "Unveiling the structure of neutron-rich Z=9 isotopes: the case of ^{25}F". Unpublished research proposal submitted to GSI Helmholtzzentrum für Schwerionenforschung. 2024 (cit. on pp. 12, 19, 21, 22).

[38] D. S. Ahn et al. "Location of the Neutron Dripline at Fluorine and Neon". en. In: *Physical Review Letters* 123.21 (2019-11), p. 212501. ISSN: 0031-9007, 1079-7114. DOI: 10.1103/PhysRevLett.123.212501. URL: https://link.aps.org/doi/10.1103/PhysRevLett.123.212501 (cit. on p. 12).

[39] K. Boretzky et al. "NeuLAND: The high-resolution neutron time-of-flight spectrometer for R3B at FAIR". en. In: *Nuclear Instruments and Methods in Physics Research Section A: Accelerators, Spectrometers, Detectors and Associated Equipment* 1014 (2021-10), p. 165701. ISSN: 01689002. DOI: 10.1016/j.nima.2021.165701. URL: https://linkinghub.elsevier.com/retrieve/pii/S0168900221006860 (cit. on p. 12).

[40] A. O. Macchiavelli et al. "Core of F 25 in the rotational model". en. In: *Physical Review C* 102.4 (2020-10), p. 041301. ISSN: 2469-9985, 2469-9993. DOI: 10.1103/PhysRevC.102.041301. URL: https://link.aps.org/doi/10.1103/PhysRevC.102.041301 (cit. on p. 12).

[41] International Atomic Energy Agency. *IAEA Nuclear Data Services: Live Chart of Nuclides*. Accessed: 2025-07-30. 2025. URL: https://www-nds.iaea.org/relnsd/vcharthtml/VChartHTML.html (cit. on p. 13).

[42] GSI Helmholtzzentrum für Schwerionenforschung GmbH. *Accelerator Facility — gsi.de*. https://www.gsi.de/en/researchaccelerators/accelerator_facility. [Accessed 16-05-2025] (cit. on p. 14).

[43] R. Hollinger et al. "Status of high current ion source operation at the GSI accelerator facility". en. In: *Review of Scientific Instruments* 79.2 (2008-02), p. 02C703. ISSN: 0034-6748, 1089-7623. DOI: 10.1063/1.2801623. URL: https://pubs.aip.org/rsi/article/79/2/02C703/1068369/Status-of-high-current-ion-source-operation-at-the (cit. on p. 13).

[44] H. Vormann et al. "High current heavy ion beam investigations at GSI-UNILAC". en. In: *Journal of Physics: Conference Series* 2420.1 (2023-01), p. 012037. ISSN: 1742-6588, 1742-6596. DOI: 10.1088/1742-6596/2420/1/012037. URL: https://iopscience.iop.org/article/10.1088/1742-6596/2420/1/012037 (cit. on p. 13).

[45] W. Barth et al. "High brilliance beam investigations at the universal linear accelerator". en. In: *Physical Review Accelerators and Beams* 25.4 (2022-04), p. 040101. ISSN: 2469-9888. DOI: 10.1103/PhysRevAccelBeams.25.040101. URL: https://link.aps.org/doi/10.1103/PhysRevAccelBeams.25.040101 (cit. on pp. 13, 15).

[46] R. Singh. "Tune measurement at GSI SIS-18: Methods and applications". In: (2014) (cit. on p. 14).

[47] GSI Helmholtzzentrum für Schwerionenforschung GmbH. *SIS18 Sections — gsi.de*. https://www.gsi.de/en/work/accelerator_operations/accelerators/heavy_ion_synchrotron_sis18/sis18_sections. [Accessed 16-05-2025] (cit. on p. 15).

[48] H. Geissel and Y. A. Litvinov. "Experiments with the FRS facility at GSI". en. In: *Nuclear Instruments and Methods in Physics Research Section B: Beam Interactions with Materials and Atoms* 266.19-20 (2008-10), pp. 4176–4182. ISSN: 0168583X. DOI: 10.1016/j.nimb.2008.05.093. URL: https://linkinghub.elsevier.com/retrieve/pii/S0168583X08007003 (cit. on p. 14).

[49] GSI Helmholtzzentrum für Schwerionenforschung GmbH. *WebHome < FRS < GSI Wiki — wiki.gsi.de*. https://wiki.gsi.de/FRS/. [Accessed 16-05-2025] (cit. on p. 16).

[50] S. Paschalis et al. "The in-beam tracking detectors of the R^{3}B experiment". en. In: (2015). Medium: Abstract Publisher: GSI Helmholtzzentrum fuer Schwerionenforschung, Darmstadt. DOI: 10.15120/GR-2015-1-MU-NUSTAR-NR-15. URL: https://repository.gsi.de/record/183947 (cit. on p. 19).

[51] M. Mager. "ALPIDE, the Monolithic Active Pixel Sensor for the ALICE ITS upgrade". en. In: *Nuclear Instruments and Methods in Physics Research Section A: Accelerators, Spectrometers, Detectors and Associated Equipment* 824 (2016-07), pp. 434–438. ISSN: 01689002. DOI: 10.1016/j.nima.2015.09.057. URL: https://linkinghub.elsevier.com/retrieve/pii/S0168900215011122 (cit. on p. 19).

[52] D. Cortina-Gil et al. "CALIFA, a Dedicated Calorimeter for the R3B/FAIR". en. In: *Nuclear Data Sheets* 120 (2014-06), pp. 99–101. ISSN: 00903752. DOI: 10.1016/j.nds.2014.07.017. URL: https://linkinghub.elsevier.com/retrieve/pii/S0090375214004694 (cit. on p. 20).

[53] M. Heil et al. "A new Time-of-flight detector for the R^{3}B setup". en. In: *The European Physical Journal A* 58.12 (2022-12), p. 248. ISSN: 1434-601X. DOI: 10.1140/epja/s10050-022-00875-8. URL: https://link.springer.com/10.1140/epja/s10050-022-00875-8 (cit. on p. 20).

[54] R. Santonico and R. Cardarelli. "Development of resistive plate counters". en. In: *Nuclear Instruments and Methods in Physics Research* 187.2-3 (1981-08), pp. 377–380. ISSN: 01675087. DOI: 10.1016/0029-554X(81)90363-3. URL: https://linkinghub.elsevier.com/retrieve/pii/0029554X81903633 (visited on 2025-09-01) (cit. on p. 23).

[55] W. Riegler and C. Lippmann. "The physics of Resistive Plate Chambers". en. In: *Nuclear Instruments and Methods in Physics Research Section A: Accelerators, Spectrometers, Detectors and Associated Equipment* 518.1-2 (2004-02), pp. 86–90. ISSN: 01689002. DOI: 10.1016/j.nima.2003.10.031. URL: https://linkinghub.elsevier.com/retrieve/pii/S0168900203027311 (visited on 2025-08-28) (cit. on p. 23).

[56] A. Blanco et al. "The SHiP timing detector based on MRPC". en. In: *Journal of Instrumentation* 15.10 (2020-10), pp. C10017–C10017. ISSN: 1748-0221. DOI: 10.1088 /1748-0221/15/10/C10017. URL: https://iopscience.iop.org/article/10.10 88/1748-0221/15/10/C10017 (visited on 2025-08-22) (cit. on pp. 23–25).

[57] A. Neiser et al. "TRB3: a 264 channel high precision TDC platform and its applications". en. In: *Journal of Instrumentation* 8.12 (2013-12), pp. C12043–C12043. ISSN: 1748-0221. DOI: 10.1088/1748-0221/8/12/C12043. URL: https://iopscience. iop.org/article/10.1088/1748-0221/8/12/C12043 (visited on 2025-09-01) (cit. on p. 24).

[58] M. Xarepe et al. "Resistive plate chambers for precise measurement of high-momentum protons in short range correlations at R 3 B". en. In: *Nuclear Instruments and Methods in Physics Research Section A: Accelerators, Spectrometers, Detectors and Associated Equipment* 1055 (2023-10), p. 168445. ISSN: 01689002. DOI: 10.1016/j.nima.2 023.168445. URL: https://linkinghub.elsevier.com/retrieve/pii/S0168900 223004357 (cit. on pp. 25, 28).

[59] J. Pereira-da-Silva et al. "Electron Driven Reactions in Tetrafluoroethane: Positive and Negative Ion Formation". en. In: *Journal of the American Society for Mass Spectrometry* 32.6 (2021-06). Publisher: American Chemical Society (ACS), pp. 1459–1468. ISSN: 1044-0305, 1879-1123. DOI: 10.1021/jasms.1c00057. URL: https: //pubs.acs.org/doi/10.1021/jasms.1c00057 (visited on 2025-07-29) (cit. on p. 26).

[60] D. Bertini. "R3BRoot, simulation and analysis framework for the R3B experiment at FAIR". en. In: *Journal of Physics: Conference Series* 331.3 (2011-12), p. 032036. ISSN: 1742-6596. DOI: 10.1088/1742-6596/331/3/032036. URL: https://iopscience. iop.org/article/10.1088/1742-6596/331/3/032036 (cit. on p. 33).

[61] M. Al-Turany et al. "The FairRoot framework". en. In: *Journal of Physics: Conference Series* 396.2 (2012-12). Publisher: IOP Publishing, p. 022001. ISSN: 1742-6588, 1742-6596. DOI: 10.1088/1742-6596/396/2/022001. URL: https://iopscience.iop. org/article/10.1088/1742-6596/396/2/022001 (visited on 2025-07-29) (cit. on p. 33).

[62] S. Agostinelli et al. "Geant4—a simulation toolkit". en. In: *Nuclear Instruments and Methods in Physics Research Section A: Accelerators, Spectrometers, Detectors and Associated Equipment* 506.3 (2003-07), pp. 250–303. ISSN: 01689002. DOI: 10.1016/S0 168-9002(03)01368-8. URL: https://linkinghub.elsevier.com/retrieve/pii/ S0168900203013688 (cit. on p. 33).

[63] R. Brun and F. Rademakers. "ROOT — An object oriented data analysis framework". en. In: *Nuclear Instruments and Methods in Physics Research Section A: Accelerators, Spectrometers, Detectors and Associated Equipment* 389.1-2 (1997-04), pp. 81–86. ISSN:

01689002. DOI: 10.1016/S0168-9002(97)00048-X. URL: https://linkinghub.elsevier.com/retrieve/pii/S016890029700048X (cit. on p. 33).

[64]   *ROOT: TMultiDimFit Class Reference*. URL: https://root.cern.ch/doc/master/classTMultiDimFit.html (visited on 2025-07-29) (cit. on p. 34).

ADDITIONAL SIMULATION STUDIES

This appendix presents additional plots obtained from the simulation studies conducted prior to the experiment. While Chapter 5 focused on the main results directly relevant for the positioning of the RPC and the development of the multidimensional fitting (MDF) functions, the figures shown here provide complementary information on the expected reaction products and the performance of the RPC. Each plot is briefly discussed to highlight its relevance and the conclusions that can be drawn.

A.1 Multiplicity Distributions

The first aspect examined in the simulations is the event multiplicity, both in the RPC and in the emitted neutrons. These observables provide a global view of the reaction environment that the detectors are expected to face.
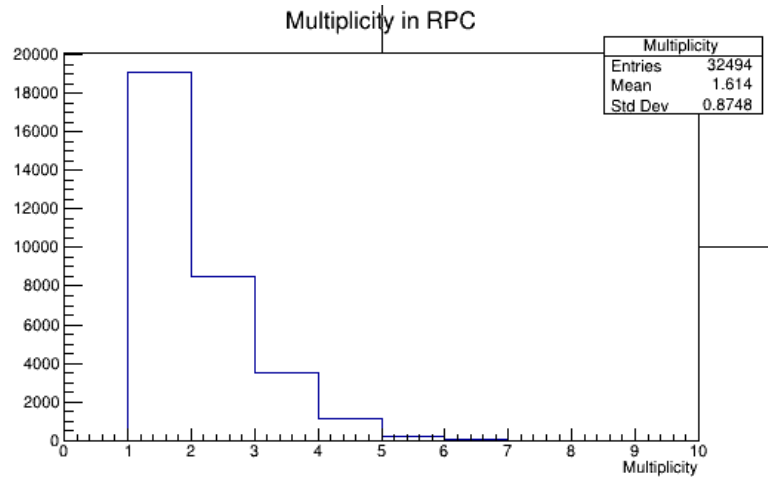

Figure A.1: Distribution of RPC hit multiplicities. The most common case corresponds to multiplicity 1, which is favorable as it simplifies the reconstruction. Multiplicity 2 events also occur with non-negligible probability, but they are typically manageable within the RPC. Events with higher multiplicities are rare and thus not expected to play a significant role.
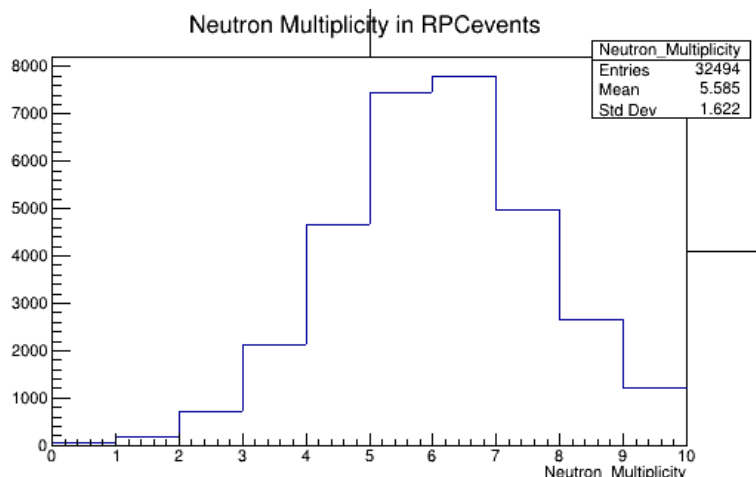
Figure A.2: Distribution of neutron multiplicities from the simulated reactions. The results indicate very high neutron multiplicities, many of which are beyond the resolution capabilities of NeuLAND. As a consequence, a substantial fraction of events will not be fully reconstructable, since part of the neutron information is lost or spread across CALIFA.

A.2 Fragment Correlations and Channels of Interest

Beyond multiplicities, the simulations were used to explore correlations between fragments and to identify reaction channels of potential interest.
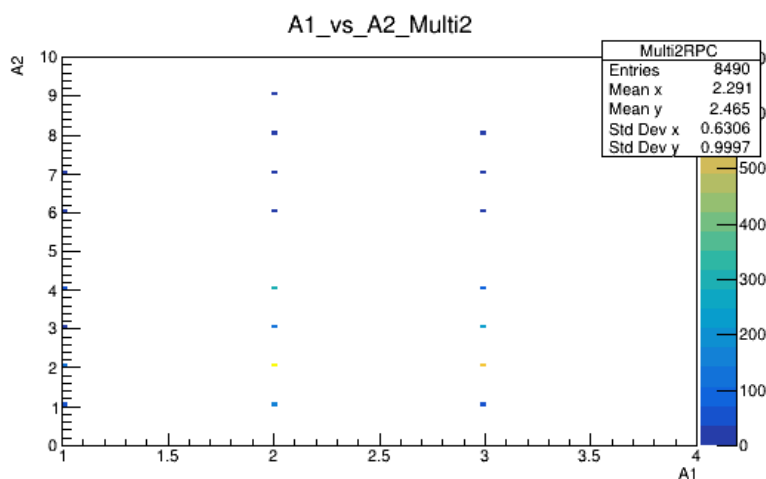

Figure A.3: Correlation between the mass numbers of two fragments reaching the RPC in multiplicity 2 events. This plot provides insight into the types of fragment pairs that dominate in such cases, which is useful for evaluating the RPC's reconstruction capabilities when handling multi-hit events.
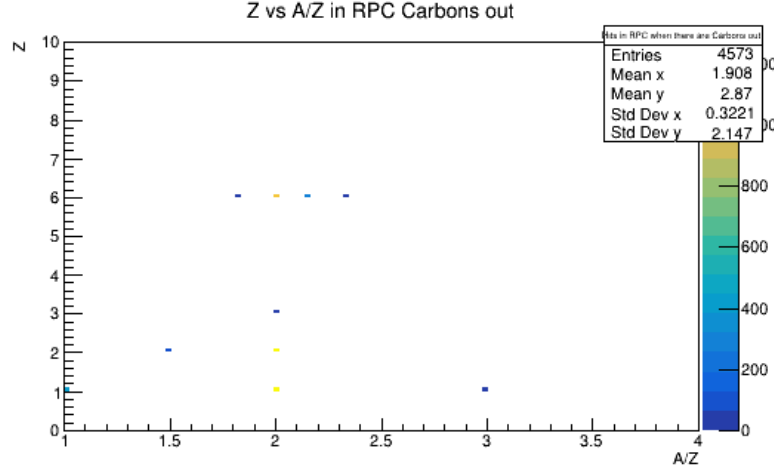
55

Figure A.4: Particle identification (PID) plot of A/Q versus Q in the RPC for events where a Carbon residue is produced. This case is of interest since one of the main fragments at the RPC are α particles, and the (p,pα) channel leading to Carbon is a promising physics case. Studying Carbon residues instead of α particles directly avoids contamination from complete disintegration channels dominated by light fragments (deuterons, tritons, and alphas).
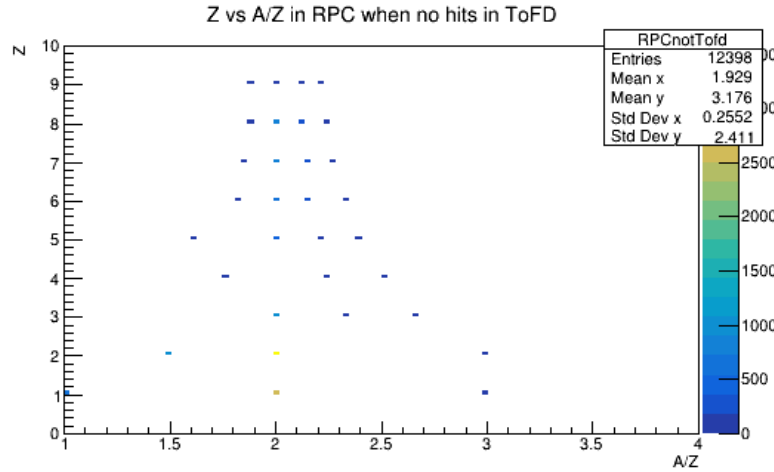

Figure A.5: PID plot (A/Q versus Q) for RPC fragments in events without a hit in ToFD. This scenario is of particular interest, as the veto condition on ToFD was later adopted in the real data analysis for the MDF application. The plot illustrates the expected distribution under this condition.

A.3 Acceptance of the RPC for $A/Q = 2$ Fragments

Since $A/Q = 2$ fragments are by far the most abundant species expected at the RPC, it is essential to assess the detector's geometrical acceptance for these particles.
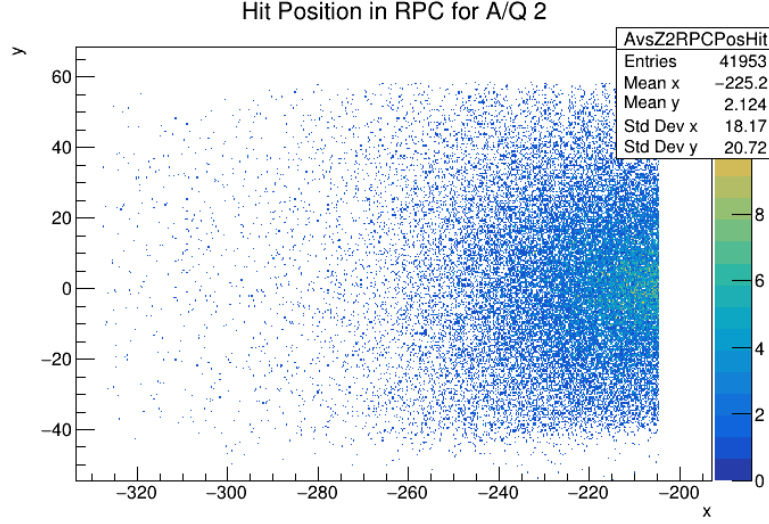

Figure A.6: Hit map of RPC signals for $A/Q = 2$ fragments. This case corresponds to the most common species expected at the RPC, and the figure provides an overview of the detector's acceptance for this population.
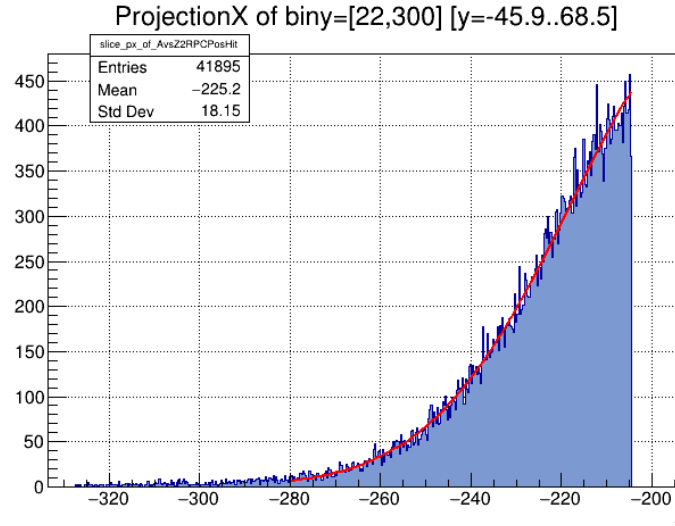

Figure A.7: Projection of the RPC hit map for $A/Q = 2$ fragments onto the x-axis, fitted with a Gaussian distribution. The fit yields a mean of -185 cm (relative to the $0°$ line) and a standard deviation of 31.8 cm. From this distribution, it is estimated that approximately 26% of the $A/Q = 2$ fragments lie within the RPC acceptance.

These simulation studies provided a baseline expectation for the experiment, serving as a reference when interpreting the real data.